Characterization of Landslide Geometry and Movement

Near Black Canyon City, Arizona

by

Hurien Helmi

A Thesis Presented in Partial Fulfillment
of the Requirements for the Degree
Master of Science

Approved April 2016 by the
Graduate Supervisory Committee:

J Ramón Arrowsmith, Chair
Duane DeVecchio
Kelin Whipple

ARIZONA STATE UNIVERSITY

May 2016

ABSTRACT

I investigate the Black Canyon City landslide (BCC landslide), a prominent deep-seated landslide located northeast of Black Canyon City, Arizona. Although the landslide does not appear to pose a significant hazard to structures, its prominent features and high topographic relief make it an excellent site to study the geologic setting under which such features develop. This study has the potential to contribute toward understanding the landscape evolution in similar geologic and topographic settings, and for characterizing the underlying structural processes of this deep-seated feature. We use field and remotely-based surface geology and geomorphological mapping to characterize the landslide geometry and its surface displacement. We use the Structure from Motion (SfM) method to generate a 0.2 m resolution digital elevation model and rectified ortho-photo imagery from unmanned aerial vehicle (UAV) - and balloon-based images and used them as the base map for our mapping. The ~0.6 km^2 landslide is easily identified through remotely-sensed imagery and in the field because of the prominent east-west trending fractures defining its upper extensional portion. The landslide displaces a series of Early and Middle Miocene volcanic and sedimentary rocks. The main head scarp is ~600 m long and oriented E-W with some NW-SE oriented minor scarps. Numerous fractures varying from millimeters to meters in opening were identified throughout the landslide body (mostly with longitudinal orientation). The occurrence of a distinctive layer of dark reddish basalt presents a key displaced marker to estimate the long-term deformation of the slide mass. Using this marker, the total vertical displacement is estimated to be ~70 m, with maximum movement of ~95 m to the SE. This study indicates that the landslide motion is translational with a slight rotational character. We

i

estimate the rate of the slide motion by resurvey of monuments on and off the slide, and examination of disturbed vegetation located along the fractures. The analysis indicates a slow integrated average landslide velocity of 10-60 mm/yr. The slide motion is probably driven during annual wet periods when increased saturation of the slide mass weakens the basal slip surface and the overall mass of the slide is increased. Results from our study suggest that the slide is stable and does not pose significant hazard for the surrounding area given no extreme changes in the environmental condition. Although the landslide is categorized as very slow (according to Cruden and Varnes, 1996), monitoring the landslide is still necessary.

DEDICATION

I dedicate this thesis to my wife who always provides me with encouragement and

support; I will not make it to this point otherwise, and to my parents for their continuous

faith in me.

ACKNOWLEDGMENTS

TABLE OF CONTENTS

LIST OF TABLES

LIST OF FIGURES

viii

CHAPTER 1

INTRODUCTION

Where there is an indication of slope instability and landslides are observed in an area, monitoring surface deformation is required to reduce the hazard. Detailed information related to the change in geometry of mass movement, fissure growth and the lateral and vertical movements are needed to specify whether the landslide is active and may pose a threat. Continuous observation and monitoring of the slide area over time is important to estimate the landslide evolution and to determine what may have triggered the slide, which can be used in landslide inventory (e.g., Niethammer et al., 2012; Turner et al., 2015). Although monitoring has an important value, geological mapping of the landslide is need to understand the long-term total deformation history of the slide.

We investigate the Black Canyon City landslide (BCC landslide), a prominent deep seated landslide located northeast of Black Canyon City, Arizona. Although the landslide does not appear to pose a significant harm to mane-made structures, its prominent morphological features and high topographic relief make it an excellent site to study the geologic setting under which the slide developed. This study has the potential to contribute to the underlying structural processes responsible for this deep seated structure, and provide insight into the landscape evolution of the area.

Over the last decade, the availability of high-resolution topography datasets have greatly improved spatial and temporal landslide mapping. Several established techniques for landslide mapping using multiple types of datasets, implemented in various terrain conditions are available. Some examples include: use of stereo aerial photographic pairs (Brardinoni et al., 2003; Van Western and Lulie Getahun, 2003; Prokesova et al., 2010),

and the use of Landsat images (Barlow et al., 2003). In addition, satellite-based synthetic aperture radar datasets are commonly used for identification of the geomorphic features in areas where vegetative cover is sparse or absent (e.g., Rott, 2009). However, all of these established methods and datasets are difficult to be implemented for landslide mapping in highly vegetated regions. The production of aerial laser scanning and terrestrial laser scanning light detection and ranging (LiDAR) topographic data greatly improve the success of landslide studies in vegetated regions regions (e.g. Van den Eeckhaut et al., 2005, 2007; Glenn et al., 2006; Cheok et al., 2002; McKean and Roering, 2004; Lichti et al., 2005; Razark et al., 2011, Ventura et al., 2011).. Unfortunately, the high cost of the LiDAR data acquisition and complication associated with it (including obtaining the permit and weather conditions) limit the usage of these data type for study in the area where the risk is not particularly high.

An alternative method of data acquisition using relatively low-cost technology (balloon, glider and unmanned aerial vehicles) is now widely used (e.g. Lucieer et al., 2013). Digital Elevation Models (DEM) with nearly centimeter accuracy can now be easily generated from images obtained by implementing structure from motion (SfM) procedures (Niethammer et al., 2012; Lucieer et al., 2013). This new affordable technique has been implemented in various fields of study including active fault mapping (Johnson et al., 2014) and landslide mapping and monitoring (Niethammer et al., 2012; Lucieer et al., 2013). The resolution of the imagery developed using the SfM method is sufficient to identify mm-m scale fissures, map the distribution and landslide geometry (surface displacement) of small (meters scale) to medium (hundreds km) scale landslides (Niethammer et al., 2012; Lucieer et al., 2013). Multi-temporal DEM data obtained from

2

this method are also useful for land-use planning and development, as shown by Lucieer et al. (2014). Comparison between the liDAR and SfM data acquisition is shown in Figure 1. We implement the SfM method using imagery obtained from balloon and UAV to generate a high-resolution topography data to map the BCC landslide, in detail.
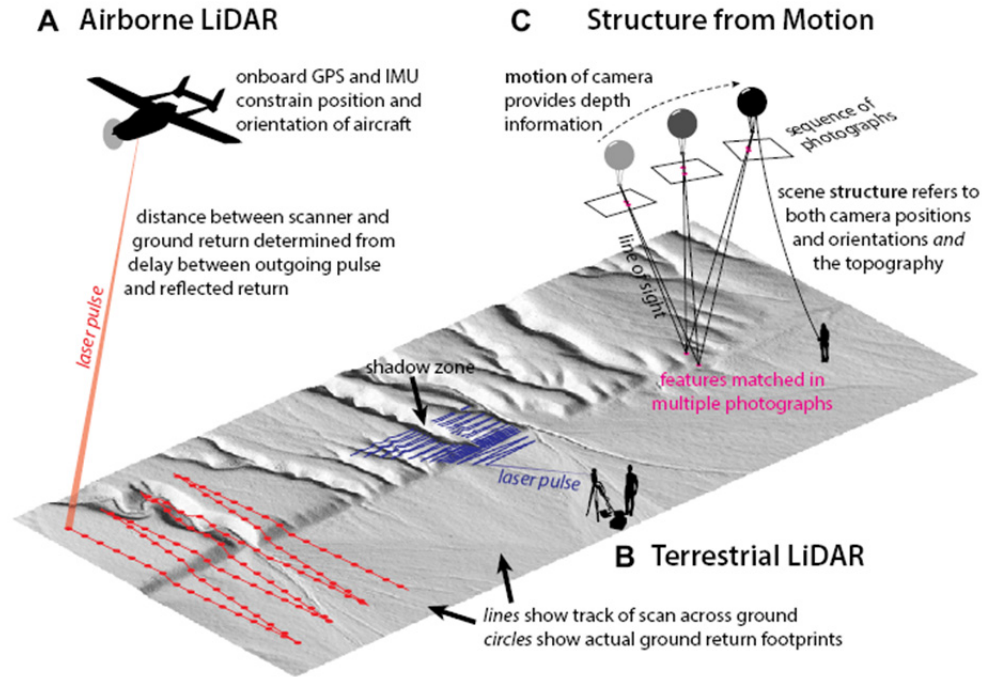
Figure 1. Illustration of three different methods of image data acquisition: airborne LiDAR Scanning (ALS), Terrestrial LiDAR Scanning (TLS) and Balloon Photography (adapted from Johnson et al., 2014)

The goal of this study is to understand the geometry and surface displacement of the BCC landslide, from which we can interpret the underlying structural processes controlling the movement of the slide. Therefore, we conducted detailed surface geological and geomorphological mapping of the landslide in order to reconstruct the deformed stratigraphy. Deformed in the BCC landslide are sedimentary strata with interbeds of basaltic lava, which is fairly common throughout the Transition zone in

3

Arizona. Thus, a better understanding of the BCC landslide has the potential to contribute to understanding the geomorphic evolution of the landscape evolution throughout the region. This study will also provide a case study where a rapid and efficient method of landslide mapping and monitoring is achievable at a relatively low cost. In addition, as the landslide is located in a populated region, this study will also contribute to the landslide hazard mitigation in the area.

In the following sections, we provide a short review of the landslide type and geometry, followed by description of the geological setting of the BCC landslide. In Chapter 2, we describe methods that we used, including: the SfM technique; field- and remotely-based surface geology and geomorphology mapping; and surface displacement measurement, followed by descriptions of the results in Chapter 3. In Chapter 4, the discussions, we examine the geometry and kinematics of the landslide, factors causing the landslide, history of movement, future movement and hazard assessment. Chapter 5 lay out some of our conclusions.

Overview of Landslide Type and Geometry

Slope failure is a common response to gravitational stresses in weak and fractured rock. The slope failures happened when a rock mass is separated from its source and moves downward until it reaches a stable slope (Varnes, 1978; Brunsden, 1984). Varnes (1978) classifies slope failure based on how the mass moved and the type of the material involved. Based on these criteria, Hutchinson (1988) refined by EPOCH, 1993 divides slope failures into five major groups: fall, topple, slides, spreads and flows depending on whether the material involved is fine and unconsolidated soil, fine-coarse grained

material, or bedrock (Table 1). Another classification by Varnes, 1978 used the movement type to differentiate the landslide into two types: translational and rotational. In the following subsection, I provide descriptions of the characteristics of both failure types.

Rotational Landslide

A rotational landslide is a slope movement, observable at the surface through series of surface ruptures that are commonly characterized by curved, concave-up basal detachment surface (Varnes, 1978)(Figure 2). The rotational events may occur along one or more sliding surfaces that can be activated in single, multiple, or successive slide events. The single rotational slide is characterized by a concavely upward-curving failure surface where the axis is parallel to contour line (Varnes, 1978). Based on the principal failure or detachment surface position, the geometry of the single rotational slide is divided into slope, toe and basal failures (from Hutchinson, 1988 in Dikau, 1996). The surface manifestation of the multiple rotational slide surfaces is similar to the single, except that the slope failure is developed into at least two or more blocks where each of the shear surfaces is tangential to the main basal slip surface (from Hutchinson, 1988 in Dikau, 1996). Where a single, shallow rotational slide occurs progressively downward along the slope the slide caused by this successive movement is called successive slides (Haefeli, 1948; Skempton and Hutchinson, 1969). In the contour map, a rotational slide is indicated by irregular, wavy contour lines (as an indication of scarp), stepped pattern, and closely or regularly spaced discontinuous lineaments (Rib and Liang, 1978).
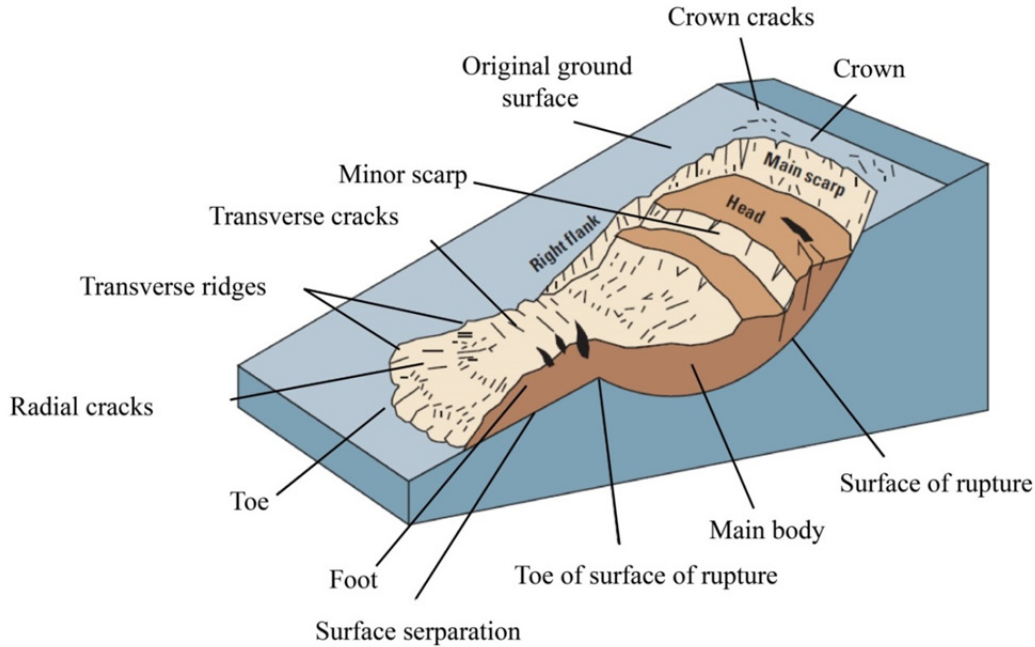
Figure 2. Diagram showing the primary features of a rotational landslide (from Highland and Bobrowsky, 2008)

Table 1. Landslide classification and mechanism (from Dikau, 1996).The table should be read from left to right.

TYPE	FORM OF INITIAL FAILURE SURFACE		SUBSEQUENT DEFORMATION
FALL detachment from	a. planar b. wedge c. stepped d. vertical	failure surface	Free fall, may break, up, roll bounce, slide, flown down slope below. May involve fluidisation, liquefaction, cohesionless grain flow, heat generation, chemical, rate effect or other secondary mechanism
TOPPLE detachment from	a. single b. multiple	a. pre-existing discontinuity b. tension failure surface	As above
SLIDE Rotational movement (sliding) on a	a. single b. successive c. multiple	circular failure surface	Toe area may deform in complex way. May bulge, override, flow, and creep. May be retrogressive
Non-rotational compound movement (sliding) on a	a. single b. progressive c. multistoried	non-circular i. listric ii. Bi-planar	Often develop a graben at the head. May have a toe failure of different type
Translational movement (sliding) on a	a. planar b. stepped c. wedge d. non-rotational	failure surface	May develop complex run-out after disintegrating. As for fall and flows

6

SPREAD			
Lateral spreading of ductile or soft material which deform in	a. layer beneath hard rock b. a weak interstratified layer c. a collapsible structure	topographic surface	Can develop sudden spreading failure in quick clays. Slope open up in blocks and gully or fissures. Liquefaction can occur and the whole spread either as a totally collapsed flow or with floating blocks and grabens
FLOW Debris movement by flow on	a. a natural complex i. unconfined ii. Channelized	-	Flow will involve complex run-out from source. May be catastrophic. May move in sheets or lobes and involve viscous or rheological mechanism
Movement by creep on		any hillslope	Creep may be gravity, seasonal, pre-failure or progressive
Rock flow (sagging, sackung) movement on	a. single b. double sided	mountain slope a. of rotational b. compound form listric bi-planar	may be slow gravity creep or early stages of landsliding, but not displaying toe deformations other than bulging
	c. stepped	discontinuity	may involve toppling
COMPLEX Movement involving two or more of the categories			

Translational Landslide

A translational landslide is a mass movement that involves translation of a slide mass along a relatively planar surface, occasionally followed by small rotational movement or backward tilting at the base (Dikau, 1996) (Figure 3). This slope failure is normally localized by a pre-existing weak interface along which the motion occurs. The surface failures commonly occur along geologic discontinuities, such as the intersection of jointing surface, fault, inclination or sub-horizontal bedding surfaces and along contact between rocks and soil. The material involved in translational landslide ranges from unconsolidated soil, loose and un-stratified sediment to large scale slabs of rock, or both determined by the slope failure and the sliding speed.
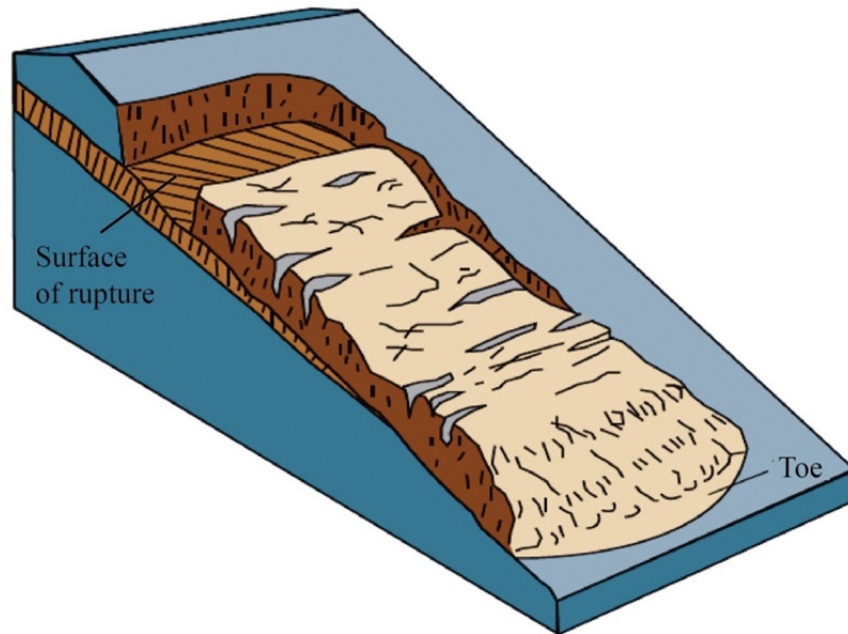
Figure 3. Diagram of characteristic features of translational landslide (from Highland and Bobrowsky, 2008)

Geologic Setting

The Black Canyon City landslide is located in Yavapai country of central Arizona, within the Transition Zone province. The zone is characterized by a northwest-trending escarpment of rugged mountainous terrain, formed by the intersection of the uplifing Colorado Plateau to the north and the tectonically subsided Basin and Range Province to the south. The boundary between the Transition Zone and the Colorado Plateau is formed by combination of structural and geomorphic processes (Spencer and Reynolds, 1989). Because of the wide variety of the topographic forms, the climatic conditions (and the character of surface processes) in this zone can be highly variable over small areas.

The tectonic evolution of central Arizona is dominated by Oligocene - Miocene crustal extensional followed by magmatism, defining a distinctive stratigraphic sequence

and structural type in the region. The geology of the study area is dominated by Proterozoic basement rocks and flat lying Paleozoic and Mesozoic sedimentary units overlain by thin layers of Pliocene to recent sedimentary rocks and volcanic units (Spencer and Reynolds, 1989) (Figure 4).

Looking into more detail on the stratigraphy in the area, the oldest sedimentary unit is the Oligocene to Early Miocene volcaniclastic sediments, which are predominately, consists of conglomeratic sandstone and fanglomerate containing pebble-boulder-sized clasts sourced from the adjacent Proterozoic basement (Figure 5). The late Oligocene to Early Miocene volcanic rocks are mostly of felsic to intermediate composition with some minor alkaline composition during a short period of time in the Late Oligocene (Coney and Reynold, 1977; Shafiqullah et al.,1980; Nealey and Sheridan, 1989; Spencer and Reynolds, 1989). The early Miocene strata are composed of interbedded early Miocene basaltic rocks, tuff, and fluvial-lacustrine sedimentary rocks (Leighty, 1997; Leighty, 2007; Ferguson et al., 2008). The late Miocene to Pliocene stratigraphy is predominatly composed of basaltic lava flows, with interbeds of intermediate silicic lavas and tuff. The Pliocene to Holocene sequence is dominated by piedmont, river and landslide deposits. The landslide deposit is composed of colluvial material formed by slope failure and is found along the lower slope of the mesas.

112°11'15"W   112°8'15"W   112°5'15"W

34°7'30"N

34°4'30"N

34°1'30"N

ARIZONA COUNTIES
Mapped Area Shown in Blue

LOCATION OF MAPPED AREA
Mapped Area Shown in Blue

Area of study

17

Fria River

Black Canyon City

Google earth

0.5   0   1 km

Explanation
Surficial Units
- d   Disturbed areas

River Deposits
- Ycr   Late Holocene active river channel deposits
- Ytr   Late Holocene river terrace and point bar deposits
- Ytr   Late Holocene river terrace deposits
- Ytr   Middle Holocene river terrace deposits
- ltr   Late Pleistocene river terrace deposits
- mtr   Middle Pleistocene river terrace deposits, younger member
- mtr   Middle Pleistocene river terrace deposits

Piedmont Deposits
- Ys   Late Holocene active stream channel deposits
- Ya   Late Holocene alluvium

- Yi   Middle Holocene alluvium
- Yi   Early Holocene alluvium
- Qk   Middle to Late Pleistocene alluvium, younger member
- Qk   Early Pleistocene alluvium
- te   Quaternary talus and colluvium, undivided

Landslide Deposits
- yls   Holocene landslide deposits
- als   Pleistocene landslide deposits
- xsl   Older Pleistocene landslide deposits

Bedrock Units
- cy   Younger conglomerate (Miocene)
- Ta   Hornblende andesite (Miocene)
- b   Basat (Miocene)   Tb₁,₂   Basalt (Miocene)

- cl   Fine-grained Chalk Canyon Formation (Miocene)
- cs   Sandstone-conglomerate facies of Canyon Formation (Miocene)
- dB   Diorite (Paleoproterozoic)
- Xg   Granitoid (Paleoproterozoic)
- Xlg   Leucogranite (Paleoproterozoic)
- Xp   Porphyritic leucogranite (Paleoproterozoic)
- Xt   Tonalite (Paleoproterozoic)
- Xtd   Tonalite-diorite complex (Paleoproterozoic)
- Xd   Diorite-metabasite complex (Paleoproterozoic)
- Xv   Felsic metavolcanic (Paleoproterozoic)
- Xs   Schist (Paleoproterozoic)
- Xts   Talk Schist (Paleoproterozoic)

Figure 4. Map showing the location of study area in Black Canyon City Arizona (blue square), the bottom figure show the location of study on the regional geologic map of the Black Canyon City and Squaw Creek Mesa City quadrangles (modified from Ferguson, et al., 2008).

10
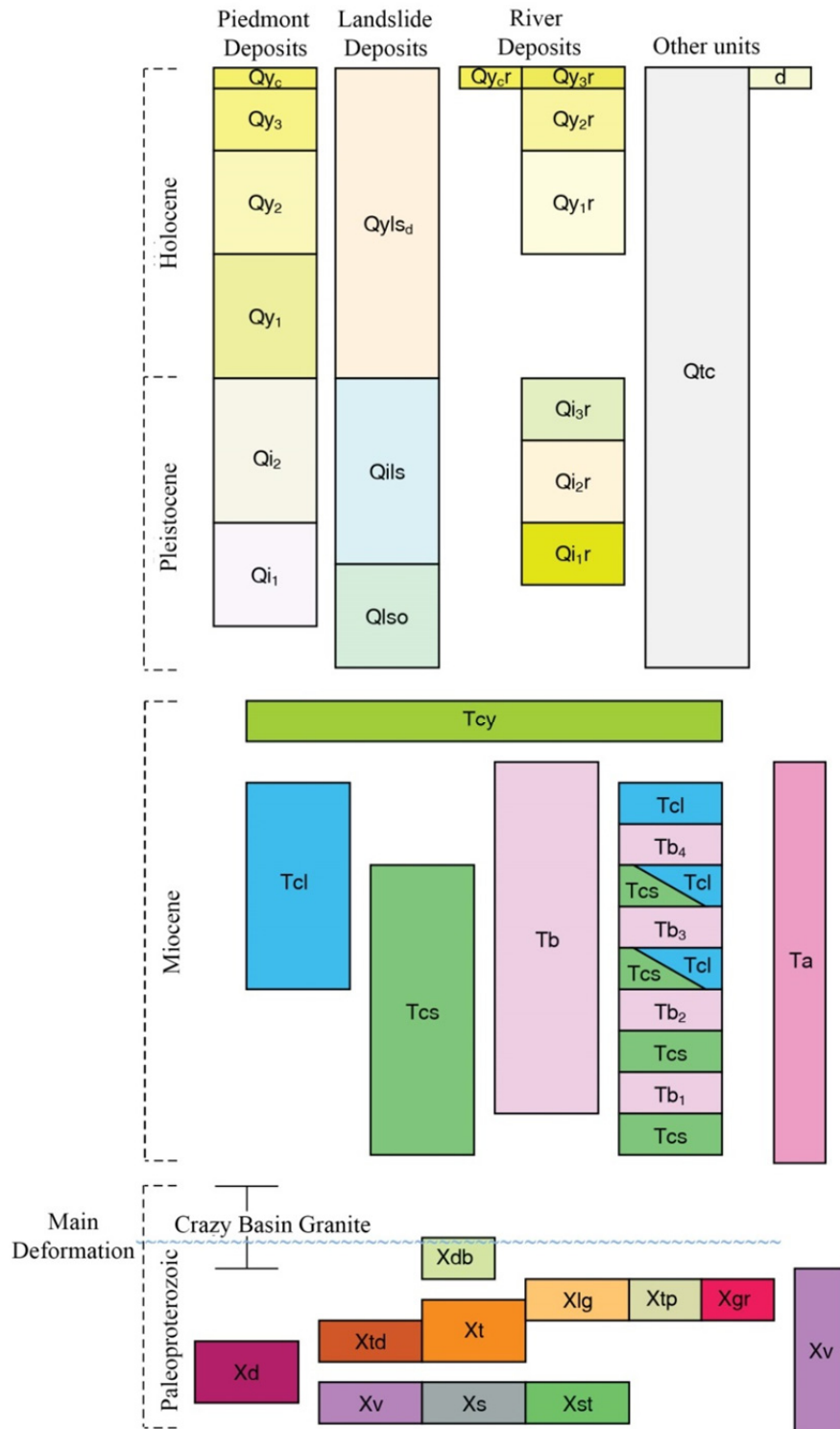
Figure 5. A simple regional stratigraphy of the Black Canyon City and Squaw Creek Mesa City quadrangles, Arizona. See Figure 4 for detailed explanation of surficial units (modified from Ferguson et al., 2008)

CHAPTER 2

METHODS

We conducted two main activities during this study: geologic and geomorphic

mapping and topographic surveying. We implemented both field and remotely-based

methods in our detailed surface geology and geomorphological mapping. We used

structural from motion (SfM) technique to generate the base map for our mapping. Along

with the mapping, we conducted a topographic survey of the previously installed

monument station using differential GPS (dGPS) to quantify any surface deformation. In

the following sections, we describe the base map generation, mapping and topographic

surveying and data analysis methods.

Basemap Construction: Structure from Motion Technique

The only available preexisting elevation data were 10-m DEMs from the USGS.

These data were insufficiently detailed for the purpose of a basemap for this study.

Therefore, we turned to SfM techniques to produce a high-resolution DEM and

orthophoto base map.

Images used for this study were taken using both balloon and UAV

(quadracopter) platforms (Figure 6). We processed the images using commercial image

processing software (Agisoft PhotoScan Professional, version 1.2.2). We pre-selected the

imagery based on their quality. The software has a relatively simple interface and

workflow to build point clouds, topography and texture model using photogrammetry

principles. We follow the procedures and parameters described by Verhoeven, 2011,

Doneus et al., 2011, and Doneus et al., 2012. The standard procedure of SfM data

processing in PhotoScan is summarized in Table 2.

Table 2. Workflow of general procedure and parameters used for SfM analysis in the
Agisoft Photoscan software, version 1.2.2.

General workflow	Alignment/reconstruction parameter
1. Add photo	
2. Align photo	- Accuracy : medium
	- Pair preselection : generic
3.Building dense point cloud	- Quality : medium
	- Depth filtering modes : mild
4.Building mesh	- Surface type : height field
	- Source data : dense cloud
	- Face count : medium (80.000)
	- Interpolation : enable
5. Building model texture	- Mapping mode : orthophoto
	- Blending mode : mosaic
	- Enable color correction : on

The first step is loading the photographs; all of the images are in a standard JPEG

format that can be easily read by PhotoScan. The photographs taken from the balloon

platform did not have any record on the coordinates of the location at the time of shooting

but the location of each photographs taken by the UAV platform are stamped (EXIF

header) with their GPS position from the quadcopter on board GPS. We did not include

photographs that are out of focus and blurry due to camera shaking. The next step is

align the photos by matching the features and bundle block adjustment, it should be noted

that the alignment is purely based on feature matching and not based on the coordinate

data embedded in the images. This process was done automatically; the software

determines the camera position and orientation from this process. A "sparse cloud" is

thus generated (e.g., Johnson et al., 2014). The sparse point clouds are then saved in

ASCII or LAS format. Poor quality photographs with large error in their relative

positions were removed to eliminate reconstruction error in the next step (Lucieer et al.,

2014).
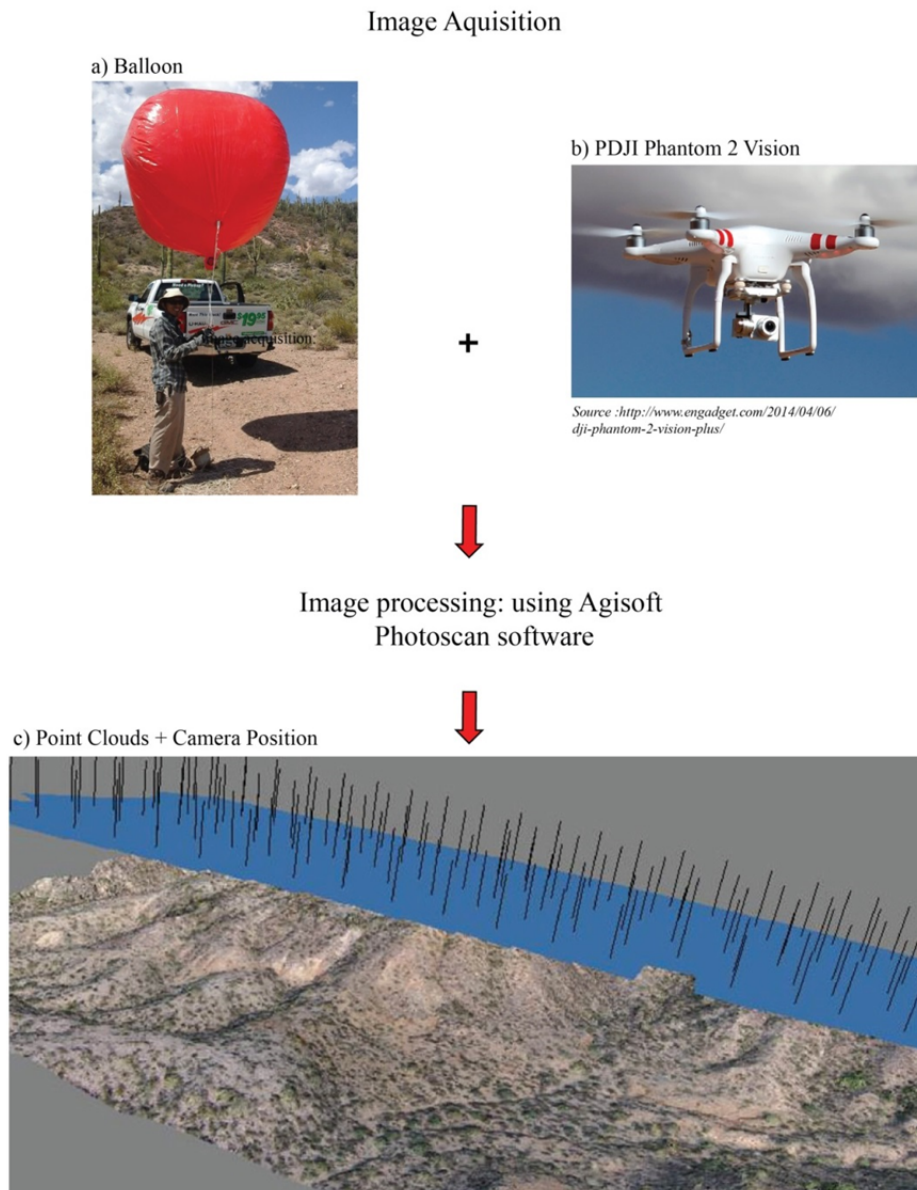
Figure 6. Diagram showing the workflow to generate point cloud using SfM procedure. The images were taken using balloon and quadcopter platform. The photos were processed in the Agisoft Photoscan software, blue square represent the camera position, red arrows indicates the steps in the workflow.

The next step is building the "dense point clouds". The calculation can be done by the software after the estimated positions of the camera have been determined (in the sparse cloud step). There are five levels of quality parameters used in building the dense point clouds. The density of the point cloud will increase with the increasing quality (Johnson et al, 2014). We generate dense enough point clouds (~17 million points) that are sufficient for our study.

The third step is building the mesh from the point clouds using parameters specified in Table 2. The processing time to build mesh was approximately 6.5 hours. The fourth step is georeferencing the 3D model using prominent markers on each of the photographs. These markers on the overlapping images are required for the next step of geometry optimization. Prior to the optimization, the relative coordinates are transformed to the actual coordinate system. We use the WGS 1984, UTM Zone 12 N. The transformation can be done in multiple ways: by using direct georeferencing (GPS camera position attached on UAV, balloon or other aerial platform) and by assigning ground control points (GCP) on the surface and measuring their coordinates from Google Earth or in the field using GPS. We use the more simple, fast, and inexpensive method of extracting the coordinates of the well-defined features from the Google Earth images. Some of the most well-defined features in the field and in the Google Earth images are the Saguaro cacti plants. Each feature is a marker point (GCPs). We identified a total of 22 of markers across the landslide area, nine of them are located outside the landslide body and three of them are within the landslide body (Figure 7a), the range of error of the georeferenced GCP can be seen in Table 3. These coordinates are then entered manually

into PhotoScan, and assigned them as markers on each photographs on the optimization procedure.

Table 3. Ground control point used in georeferencing the point cloud data.

Label	X error (m)	Y error (m)	Z error (m)	Error (m)	Projections	Error (pix)
M1	-0.240	0.552	6.250	6.279	12	0.121
M2	-0.590	0.131	5.804	5.835	8	0.136
M3	-0.685	0.556	4.928	5.006	10	0.075
M4	0.031	0.249	-1.955	1.971	11	0.262
M5	-1.052	-1.517	6.848	7.092	14	0.114
M6	2.022	2.602	-2.188	3.955	7	0.203
M7	5.359	3.894	2.339	7.025	9	0.189
M8	0.239	-3.929	3.064	4.989	10	0.365
M9	2.177	1.836	-1.556	3.246	13	0.600
M10	1.228	0.842	-0.401	1.542	7	0.027
M11	-1.065	0.520	0.391	1.248	15	0.120
M12	-1.169	0.681	1.552	2.059	24	0.082
M13	1.974	2.417	-0.830	3.229	7	0.109
M14	-0.058	-0.448	-8.695	8.707	7	0.069
M15	0.091	0.715	-3.523	3.596	10	0.027
M16	-0.365	-0.969	-4.228	4.353	3	0.034
M18	0.122	2.739	6.374	6.938	19	8.932
M19	0.295	2.026	-1.638	2.621	16	0.213
M20	-2.227	0.021	4.425	4.954	10	0.126
M21	1.506	-2.348	-6.594	7.160	34	0.341
M22	0.447	0.252	0.187	0.546	14	0.398
M23	1.038	0.393	-2.399	2.644	10	0.086
Total	**1.599**	**1.784**	**4.217**	**4.850**	**270**	**2.381**

After the first optimization procedure, steps 2, 3, and 4 are repeated before the final step of building the model texture. This multiple step georeferencing method has improved the previous work methods and reducing the processing time significantly, especially during the early step of images matching features (Johnson et al., 2014). The disadvantages of this method are sometime it requires a lot of time to identify the markers

16

and it may generate a less accurate digital elevation model (DEM). However, by using this method, we are able to achieve a 20-cm resolution DEM, sufficient for our study (Figure 7b). To test the quality of the DEM, we overlay the model onto Google Earth platform. The features and topography of the model fitting well on the topography and features identified in the Google Earth (Figure 8b).

The final step of the SfM data processing is building the model texture to generate the orthophoto. It is a process of translating the overlapping original images into the 3D surface model. The step relies on the previously built dense point clouds and their geometry. The generated orthomosaic is projected into the planimetric view in the specified coordinate system.

All of the data including those measured in the field (e.g., strike, dip, fault/joint measurements) and those that are generated by the SfM procedures in PhotoScan (i.e., DEM, orthomosaic) are imported to AcrMap 10.2 (GIS) software. Derivative maps, such as contour, hillshade and slope were generated, interpreted and used as the base map of this study. The contacts of lithology, faults, and morphologic features are plotted in the GIS system.
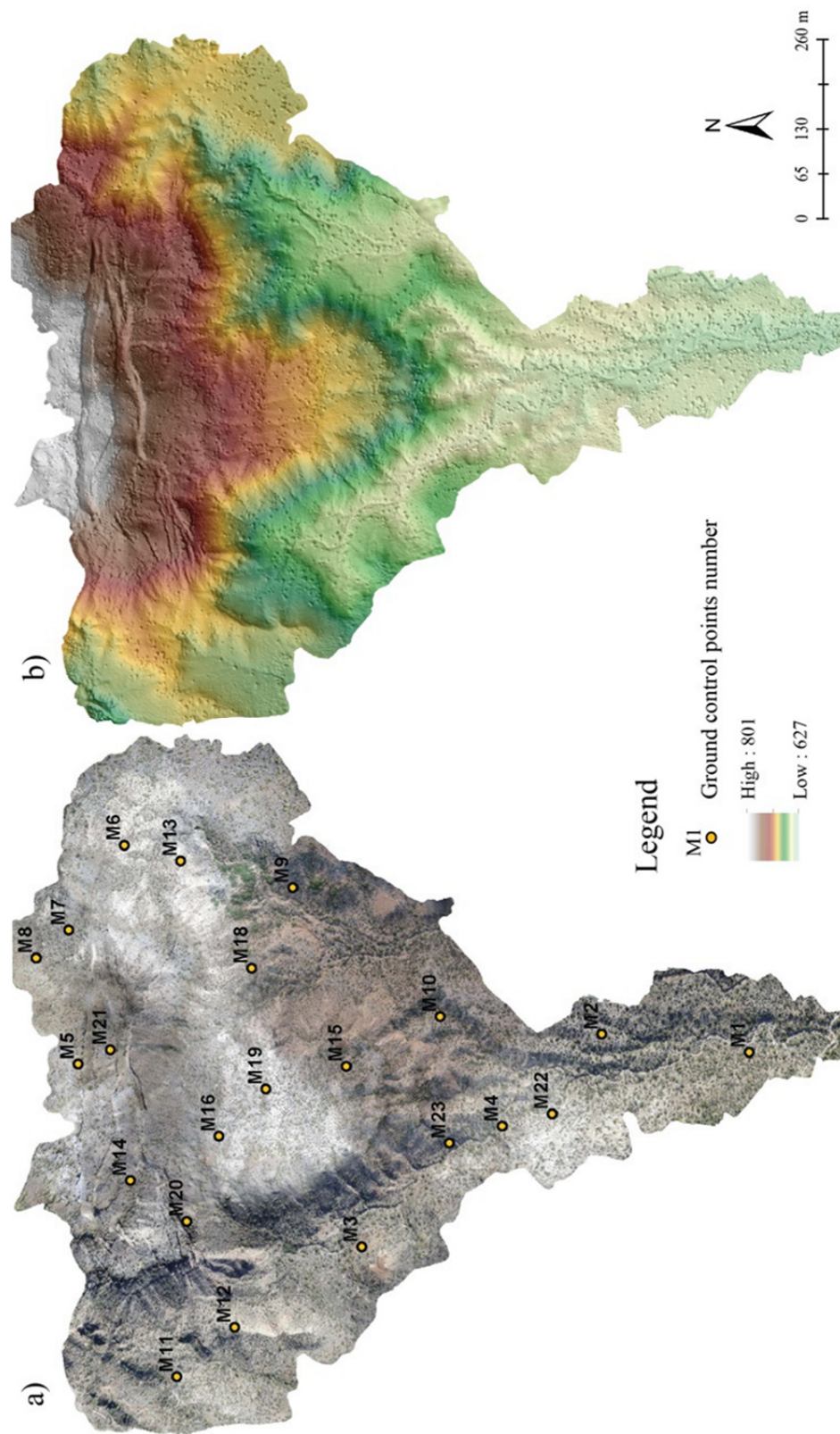
Figure 7. Example of high resolution imagery data generated from combination balloon and quadcopter photogrammetry of the study area. a) The orthophoto, yellow circles are ground control points (GCPs) used for georeferencing the data. b) The 20 cm-resolution DEM of the study area overlaid on the hillshade map.
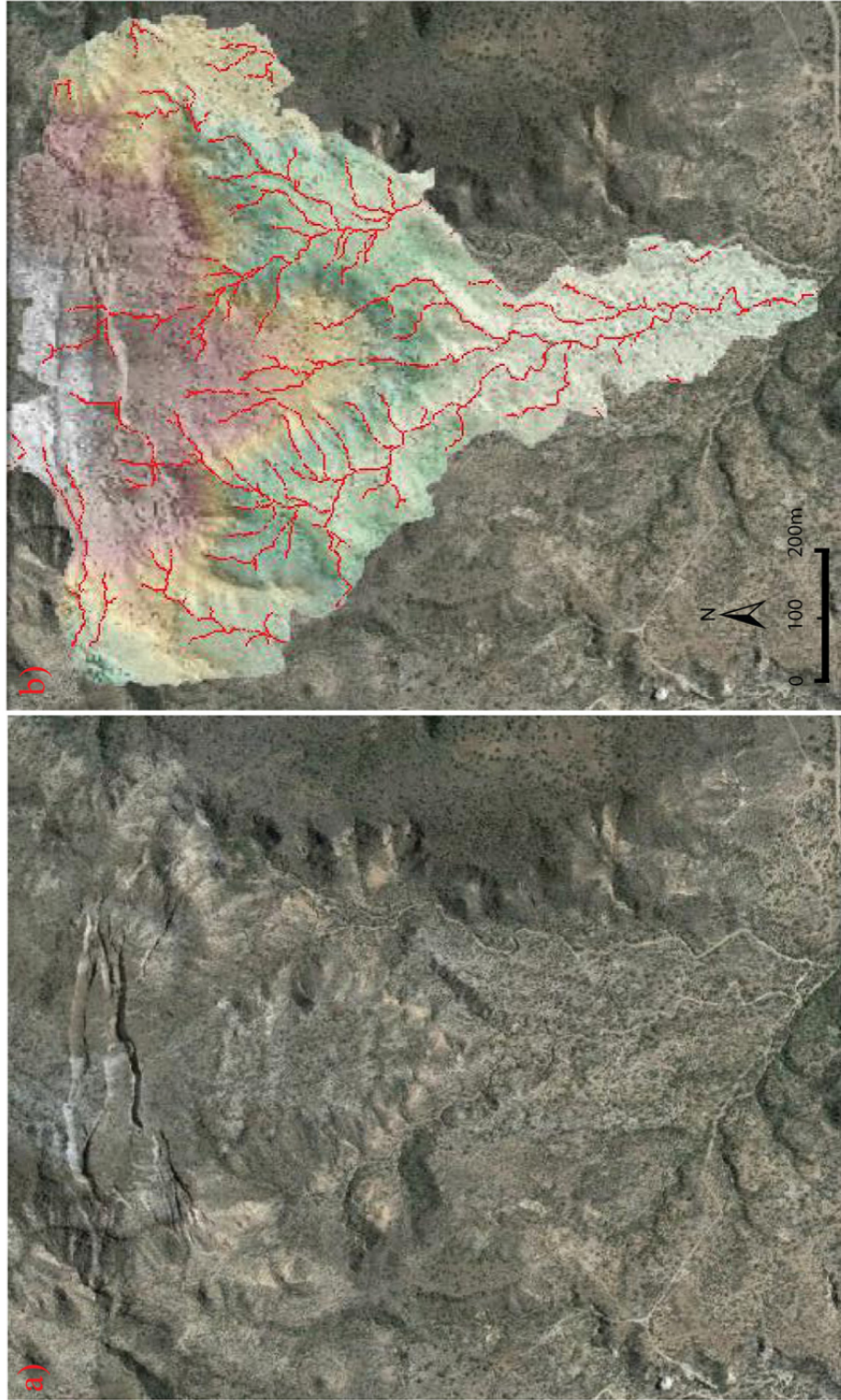
Figure 8. Hillshade map+DEM of the study area overlain on top of Google earth imagery showing that the feature and topography of the model fit well with the topography and features identified in Google earth.

Field and Remotely Based Surface Geology and Geomorphology Mapping

The geology of the Black Canyon City landslide and its surrounding region was mapped by Leighty (2007) and was refined by Ferguson et al. (2008) at a scale 1:24,000 map (Figure 4). For the purpose of the study, we needed to map the feature in a cm-m scale and with a more detailed mapping method. We begin with remotely based mapping, followed by field-based mapping; all of the mapping was then compile into the GIS system using ArcGIS.

The first step was to map the landforms on the DEM and its derivative maps, such as slope map, hillshade and contour map. We use the objective mapping method developed by Savigear (1985). It emphasizes changes of slope (Figure 9). We identify and map every topographic break as well as the type and shape of the slope changes. Systematic changes of slope might represent structural or lithological differences that can be confirmed during field mapping.

In general, lithologic contacts are well-represented in the orthophoto based on the changes in surface tones. We delineate the contacts that are clearly visible from the imagery leaving out the more ambiguous contacts for verification during field mapping. During the field work, we confirmed and refined the lithologic contacts, measured the strike and dip of the layers (both those that are still intact outside the slide mass and those that are displaced by the slide). We also measured the orientation of fractures and fault planes. In addition, we measured stratigraphic thickness of the units involved in the slide and develop a stratigraphic column.
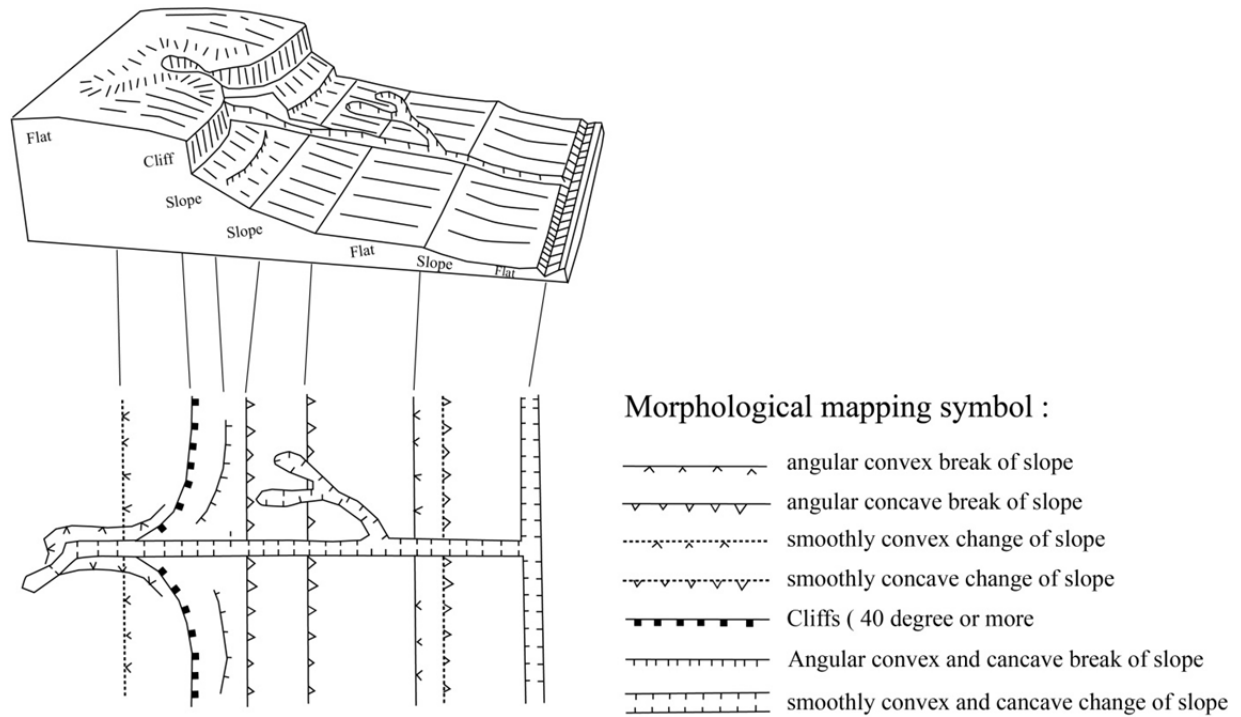
Figure 9. Morphological mapping aspects and their symbol for detailed morphology mapping (modified from Savigear, 1965).

Monitoring Landslide Displacement

GPS survey stations were previously installed through the landslide body in 1998. These survey stations are including 17 bench-marks and 1 instrument station, where 4 of them including instrument station were placed outside of the slide area within stable zone, whereas the rest of these points are located through the landslide body. At that time, the benchmarks was established and measured using a total station, generating local coordinates system of each point. In February 2016, we resurveyed these points using a Leica 2100 differential Global Positioning System (dGPS) . We measured all 15 survey stations including the instrument station and recording the global coordinates system of

21

all points. The purpose was to identify any indication of surface movement since survey

points were installed in 1988.

We implement simple transformation to the old data into global coordinate system

of WGS 1984 using the simple rotation equations as follow:

$$x = x'\cos\alpha - y'\sin\alpha$$

$$y = x'\sin\alpha + y'\cos\alpha$$

where x and y is the new coordinates, x' and y' is the old coordinates, and α is the degree

of rotation (obtained from comparing the old and new data) (Figure 10). We calculate the

difference of the position (east, north and height component) relative to instrument

station and BM1, which is located in a stable part of the landslide.
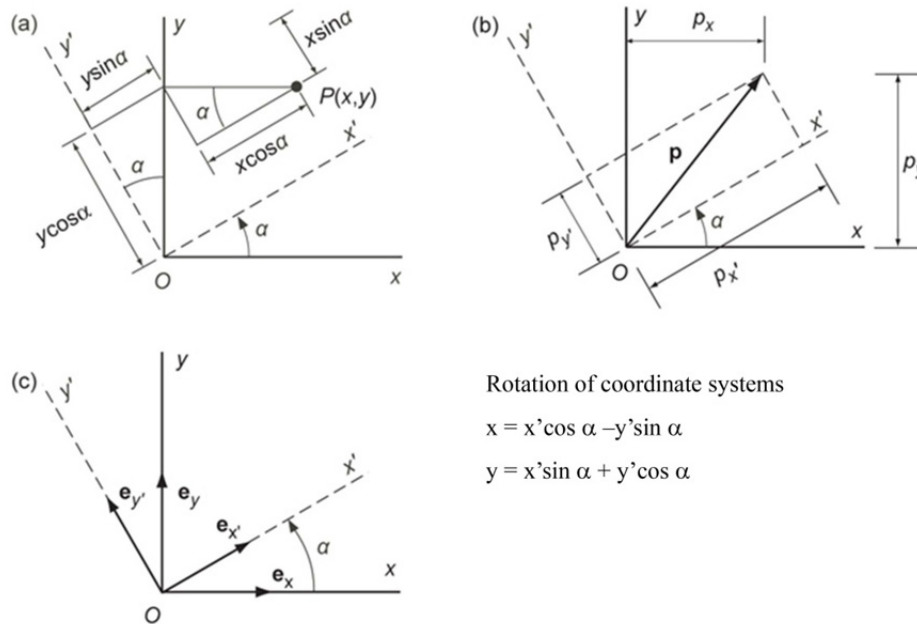
Figure 10. Rotation of coordinate systems (—From Pollard and Fletcher, 2005, Figure
2.8).

CHAPTER 3

RESULTS:

ACCURACY ASSESMENT OF THE DEM &

DETAILED GEOLOGY AND GEOMORPHOLOGY MAPPING

The SfM technique that we implemented successfully modeled the topographic features at varying scales, which was critical to accurate surface geological and geomorphological mapping. The accuracy assessment of the DSM is described in the following subchapter, which is then followed by description of the landslide characteristic (from remote- and field-based mapping) and descriptions of the results from the surface displacement measurements.

Accuracy Assessment of the Digital Elevation Model

During the images acquisition, we used Pentax WG-2 and Phantom Vision 2, which both cameras that we used has similar resolution of 4608 x 3456 megapixels on each image. Within each image, averages of 123,102 tie feature points were detected by Agisoft PhotoScan 1.2.2. A sparse point cloud was generated, and further processes yielded a denser point cloud, increasing the number of points from ~120 thousand to ~17 million points. The imagery covers an area of around 0.6 km^2 resulting in an average ground point density of almost 25 points/m^2. Our data processing produced a good quality dense cloud but manual editing of the point cloud was necessary.

The SfM method does not necessarily require the use of ground control points (GCPs) to create the mesh because it can work in a relative internal coordinate system. Consequently, the resulting point clouds and mesh are not scaled, translated or rotated

23

and thus are not related to the global coordinate system. For some applications where relative spatial coordinate is sufficient, this may not be a problem, but for my study, the spatial reference to the established coordinate system is important to precisely locate the landslide features and to compare our measurement with the pre-existing data. We are using coordinates of objects that are recognizable both in the imagery and in the field acquired using both handheld GPS and Google Earth imagery to georeferencing the dataset. The method worked well for this dataset, automatic assessment by the Agisoft Photoscan exhibit total error of less than ~5 m was achieved, which is enough resolution for the purpose of our study. The generated digital elevation model (DEM) and orthophoto are shown in Figure 7.

Topographic features of varying scales were clearly visible in the dataset. We were able to comparably distinguish the features that we identified in the imagery in the field with high confidence. When viewed in the GIS software as hillshade (colored by elevation) overlaid by DEM, the modeled area successfully demonstrated the fine (meter) scale surface features of the landslide and surrounding landscape (Figure 8b). Vegetation was also clearly defined. Some of the vegetation also appears in the DEM as clumps, covering the topography, but because they are not obscuring the observation, the vegetation removal process was not necessary. Comparison between the DEM generated from the SfM and the 10-m DEM USGS is shown in Figure 11 and highlights the improvement of the quality and resolution of the topography data.
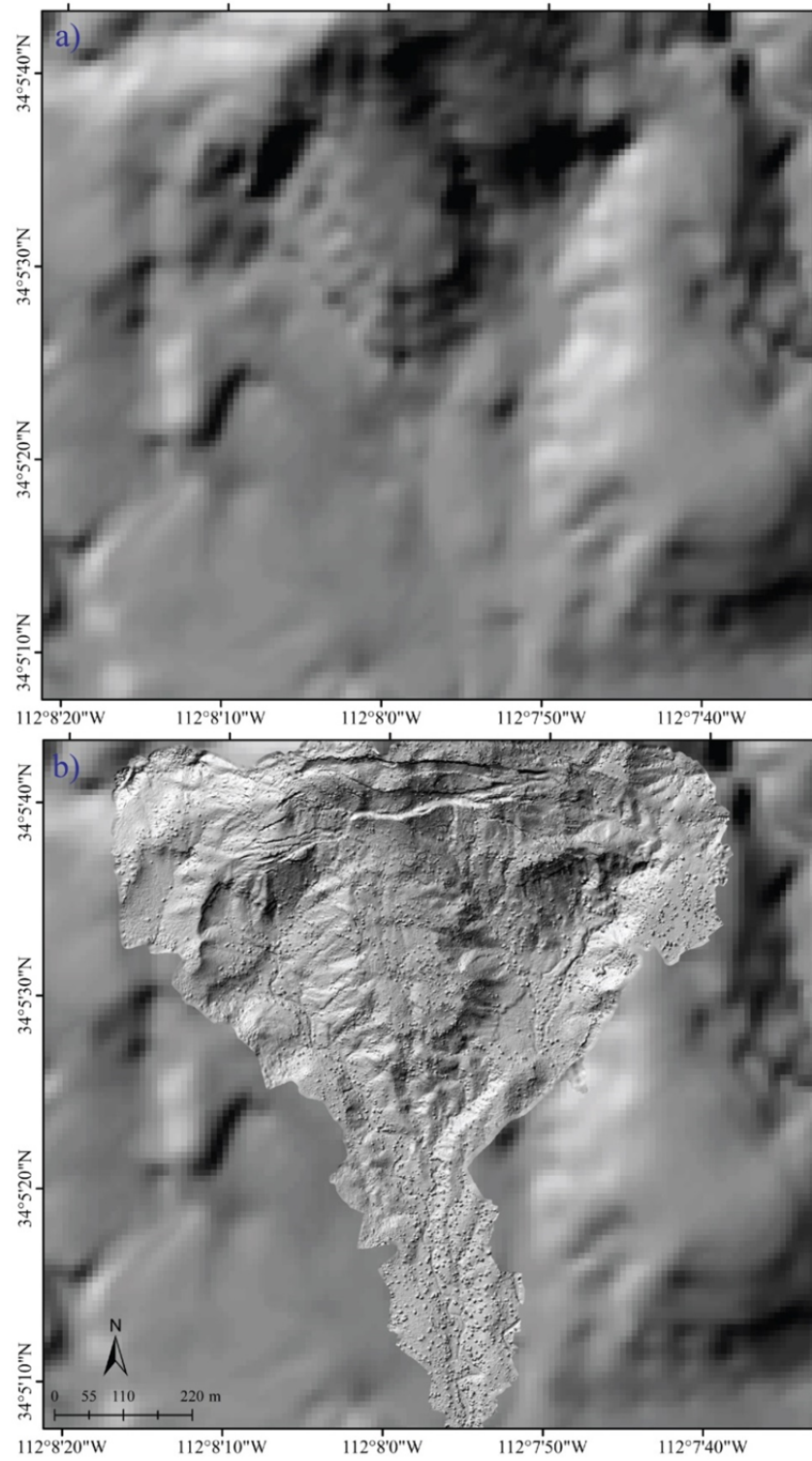
Figure 11. Comparison of the hillshade generated from the DEM from the older 10-m resolution USGS DEM (a) and the 20-cm resolution DEM resulted from this study (b).

Local Stratigraphic Units

Based on the field mapping, the sedimentary sequence in which the landslide is developed includes multiple basaltic lava flows, conglomeratic sandstone, clayey sandstone and alluvium (Figure 12). There is a general variation in composition of the disrupted layers of rocks that has been useful in correlating landslide deposits with their source location. The materials exposed in the main scarp (the original, undisturbed section) are a complex array of volcanic and sedimentary rocks of various compositions comprised of the Miocene Hickey Formation (Figure 4 and 5) (Ferguson et al., 2008). At the top of the section is intercalation of altered light gray and red brown basalts and called as series of upper light gray and red brown basalt. Below the basalts is the upper conglomeratic sandstone. These units conformably overlie altered massive middle red brown basalt. Conformably below the middle red brown basalt is the lower conglomeratic sandstone, lower light gray-greenish basalt, and clayey sandstone with thin of interbedded light-gray pumiceous sandstone (unweathered) within it. Right below the clayey sandstone is the oldest unit exposed in the area is the pumiceous sandstone unit (Figure 13).

The rock exposed in the south of the landslide area (below the landslide toe) is white to light gray colored pumiceous sandstone of the upper Chalk Canyon formation which is stratigraphically older than the Hickey formation (Leighty et al., 2007) (Figure 4 and 5). The sandstone is located mostly on the southern part of the study area. The outcrop expose at the bottom of the river and at the channel wall. The bedding is gently dipping, at least 1.5 meter thick and mostly covered by thick terrace deposits. The pumiceous sandstone is unconsolidated, well sorted composed of fine grained pumices,

tuff and lithic fragment (see Figure 13 for a more detailed descriptions of this unit). This sandstone absorbs water very quickly when tested in the field; indicate high porosity and it is conformably located below the clayey sandstone. Contact between these units mark a contrast between a permeable and impermeable layers, and is suspected as the slip surface of the landslide.
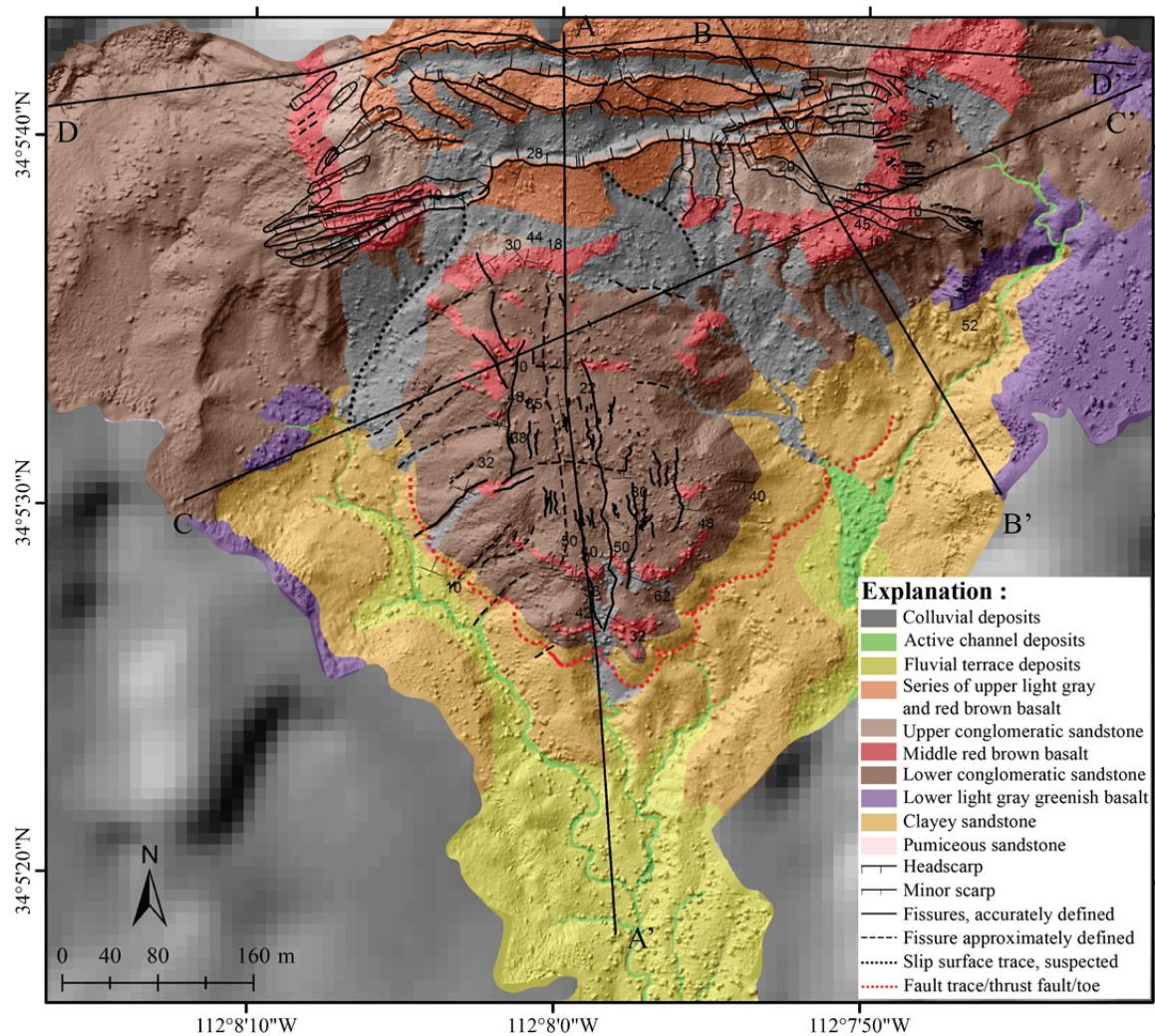
Figure 12. Geologic map of the landslide region show the fractures distribution and rock unit contacts. The material involved within the slide consist of series of upper light gray and red brown basalt, upper conglomeratic sandstone, middle red brown basalt, lower conglomeratic sandstone. The base of the slide is located within the clayey sandstone unit. The lower light gray greenish basalt unit (purple colored) is only localized at the

edge of the landslide. The black lines show the locations of cross section lines shown in Figure 30

Age	Formation	Unit	Unit Thickness	Lithology	Description
Holocene	Quarternary Deposits				Quarternary deposits are classified into fluvial and colluvial deposits; The fluvial deposit is composed by active channel and fluvial terraces deposits. The fluvial terrace deposit is characterized by moderate to well consolidated silt, fine to coarse sand, gravel and pebble. It is moderately - well sorted. The thickness is about 2 -5 m and is located within the main channel. The colluvial deposit is characterized by undifferentiated debris materials, with angular-sub angular, fragments, poorly sorted, consist of the eroded material from Chalk Canyon formation and Basalt mostly reworked from the landslide debris nearby. It is accumulated in the area near the landslide toe, along the main scarp and on the downhill area of the slide.
		Landslide Deposits / Fluvial Deposits	~8 / <5 / <2	Colluvial	
Middle Miocene	Hickey Formation	Tb (Basalt)	42 - 46	Series of upper light gray and red brown basalt	A series complex flowsheet of basaltic-andesite units, consist of interbedded light gray basalt unit at bottom and capped by red bown basalt. The light gray basalt is aphanitic-vesicular-porphyritc, contain of plagioclase (5 % < 2 mm), olivine (7 %, < 2 mm) and pyroxene (3 %, < 2 mm) as phenocryst, the outer structure is characterized by pasive structure with some amydgaloidal structure (vehicles filled by calcite and olivine Red brown basalt is characterized by porphyritic, contain olivine (7 %, < 2 mm) and pyroxene (2 %, < 2 mm) phenocrist , structure is characterized by platy columnar joint with massive structure in the interior body.
		Tcs	10 - 14	Upper Conglomeratic Sandstone	Upper conglomeratic sandstone, very fine to fine grained, unconsolidated and friable. There is a red brown color of baked zone in the contact with the overlying basalt unit.
		Tb (Basalt)	8 - 12	Middle red brown basalt	Red brown basaltic-andesite unit, aphanitic to porphyritc, contain of olivine phenocrist (8 %, < 2 mm) and pyroxene phenocrist (2 %, < 2 mm), characterized by shear zone at the flow base, massive structure in the interior body. It has a greenish gray fragmented surface on top (clinker surface interior). This unit appears to be altered and oxidized.
		Tcs (Correlate to Sandstone-Conglomerate facies of Chalk Canyon Formation)	40 - 45	Lower Conglomeratic Sandstone	Lower conglomeratic sandstone unit, poorly sorted, matrix supported with subanguluar to sub rounded clasts that reach up to 70 cm in diameter. The clast is consist of felsic and mafic granitoid rock (35%), basaltic-andesitc rock (55%), and quarzt, calsedon and metavolcanic rock (15%). In general, the beds are normaly graded. Less than 3 m of reddsih orange in the upper part unit is representing a baked zone contact with the overlying basalt.
		Tb (Basalt)	8 - 12	Lower light gray greenish Basalt	A single flow of slightly altered light gray greenish basaltic lava, jointed interior structure, vesicular-porphyritic and amygdaloidal texture with some calcite filled vesicles, composed of altered olivene (5 %, < 2 mm) and plagioclase (< 3 %) phenocryst.
		Tcs	20 - 24	Cayey Sandstone	A thicked bed of unconsolidated clayey sandstone, red brown color, very fine to fine grained, friable, consist of interbedded of unconsolidated siltstone, mudstone, and clay material. Interbedded pumiceous sandstone at the lower part of this unit.
Early Miocene	Upper Member of Chalk Canyon Formation	Tcs	>25	Pumiceous Sandstone	White to light gray unconsolidated pumiceous sandstone, matrix supported, moderately sorted, composed of fine grained subangular-angular pumice, tuff, and lithic.

Figure 13. Local stratigraphic column of the rock units identified in the Black Canyon landslide area. We use stratigraphic nomenclature described in (Ferguson et al, 2008).
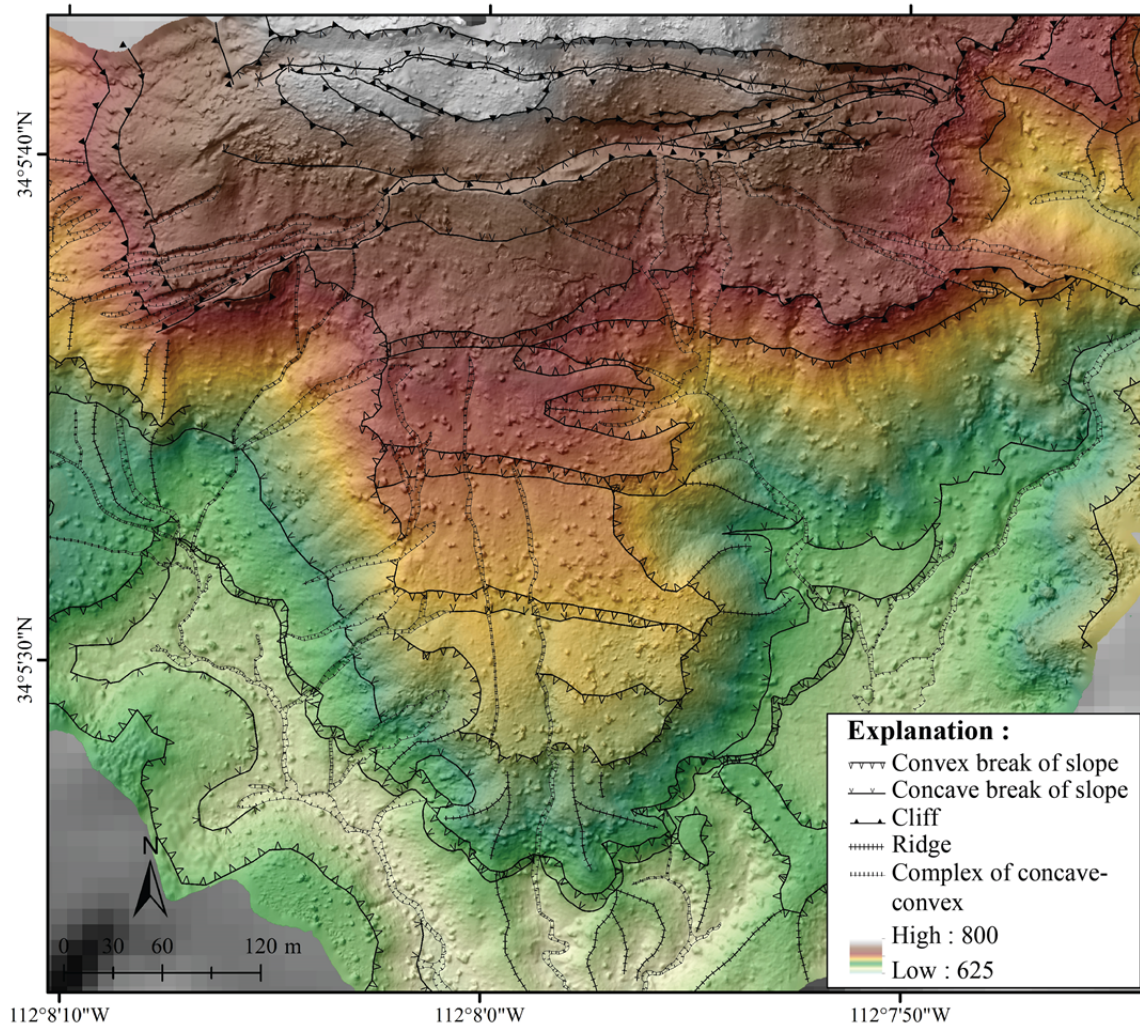
Figure 14. Morphologic map of the BCC landslide. The mapping was mainly conducted by mapping slope breaks as proposed by Savigear (1985).

The youngest units in the study site include active channel, river terrace and colluvial deposits. The active channel deposits consist of unconsolidated, poorly sorted, very fine-coarse sand-cobble materials. This unit is located within the active channel and incised ~0.4 m – 2.5 m of the terrace deposits. At least two terrace deposits were identified in this area; the upper terrace unit is exposed at ~0.8 – 10 m above the main channel while the lower terrace deposit is less than 0.8 m from the channel floor. The

upper terrace deposit has a gentle slope and consists of unconsolidated sand, pebble

cobbles with a poorly developed desert pavement. This unit is covered by sparse to

moderate vegetation. The lower terrace consists of unconsolidated silt, fine to medium

sand, pebbles and cobbles. The colluvial deposits were identified at the base of the graben

along the main head scarp, and at the margin along the toe. The colluvium consists of

debris of basalt and other Hickey Formation fragments from the upper slope and form

talus deposits. Based on the physical and field characteristic of the basalt in the study

area, I categorized the basalts into three different units as shown in Table 4.

Table 4. Field characterization of the basalt units

Units	thickness (m)	Color	Structure	Alteration	Comment
Lower light gray greenish basalt	~ 8-12	Light gray-greenish	Vesicular-porphyritic and amigdaloidal structures	Low to Moderate weathering and alteration (chlorite clay alteration)	Single basalt flow unit, interbedded within the sedimentay rocks unit
Middle red brown basalt	~ 8-12	Red brown	Platy jointed (semi columnar joint)	Moderate to high alteration (iron oxide alteration	Single basalt flow unit overlying thick lower conglomeratic sandstone
Series of upper light gray and red brown basalt	~ 42-46	Light gray and red brown	Masive, porphyritic-vesicular amigdaloidal structure on the light gray basalt and platy columnar joint on the red brown basalt	Moderate to high weathering and alteration (iron oxide alteration on the red brown basalt and chlorite clay alteration on the light gray basalt)	Consist of multiple basalt flow sheets, basalt, basaltic-andesite and rhyolite. Occupy the top of the mesa (crown area). Thin tuff layer occurred at the contact between the light gray and the red brown basalt.

Morphological Features of the Landslide

The BCC landslide shows remarkable morphologic features both in the aerial imagery and in the field (Figure 4). I mapped these features using both field- and remotely-based mapping method. The remotely-based mapping was based on the orthophoto and DEM (with its derivative maps) followed by field-checking to confirm the mapped features (Figure 14).
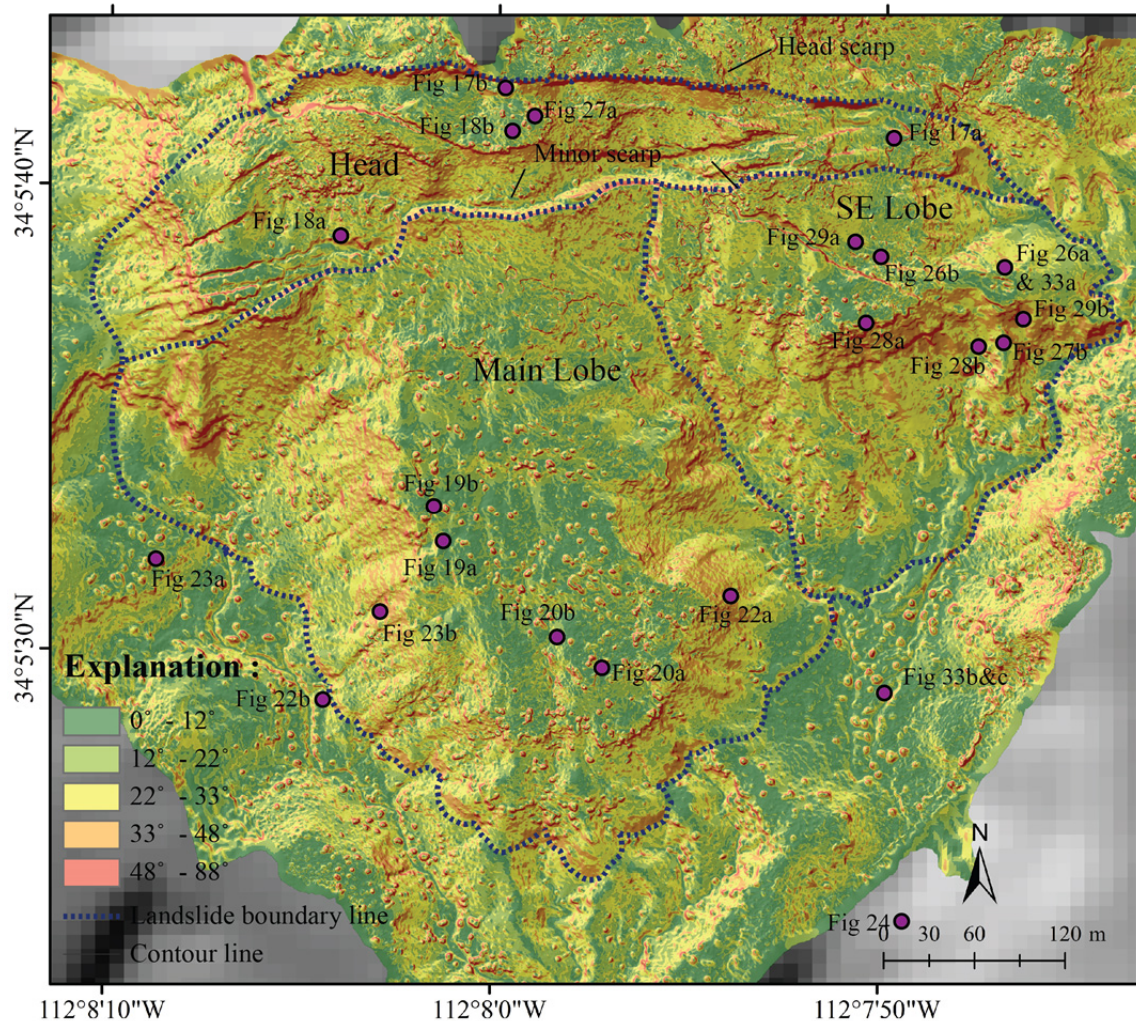
Figure 15. Slope map of the landslide generated from the SfM-DEM, with the 10-m USGS DEM on the background. The slope map highlights the distributions of scarps and large open fractures as it is characterized by steep slopes (warmer color). The blue dashed line is representing the landslide boundary; the purple circles show the location of photographs taken during the fieldwork.

31

The landside is about 0.6-km long and 0.5-km wide with a nearly symmetrical form that extends from an elevation of ~795 m at its proximal end and slopes gently to an elevation of ~ 653 m at its distal edge. Based on the interpreted stratigraphic cross sections, the thickness of the slide mass in the proximal area is ~85 m at the center and ~55 to 75 m at the edges. The slide mass in the distal region is 55 m thick at the center and ~35 to 40 m on its lateral edges. The total volume of the deposit is estimated to be ~12 x 10^6 m^3. The BCC landslide can be divided into three main zones based on its morphology: the head, main lobe, and Southeast (SE) lobe (Figure 15).

Zone A: Head

The area within the head and in the crown is rough with sparse to moderate vegetation. The most prominent surface features observed within the head area are scarps that are associated with extensional structure such as normal faults and tension crack (Figure 16). Two E-W trending main scarps were observed along with few SW-NE trending minor scarps. The E-W trending scarps are approximately ~470 m in length with maximum local relief of ~14 m (Figure 16). The highest point of the scarps is at 777 m above sea level. The SW-NE minor scarps are ~469 m long, have a maximum relief of ~7 m with a maximum elevation of 758 m. Both the main and minor scarps are represented in the morphology as a steep-almost vertical cliffs formed by normal faulting as the block mass moved and stretched horizontally downslope (Figure 14). The downhill movement of the hillslope along these faults created a local graben- and horst-like morphology, bounded by the faults (Figure 12). The grabens are represented by a pair of concave curvatures in the morphology map and are filled by talus sediments (Figure 17a,

32

and b). They reach a maximum of ~140 m wide and ~20 m minimum of lateral

separation. Several horsts like morphology that are located between two of the main

grabens were tilted. The topographic surface that are located near the western edge of the

scarp has been tilted toward the toe of the slide (south) at approximately 22˚ while the

one that located near the center of the main scarp is tilted ~34˚ and appears to sinking

down below the top surface of the main graben. The difference in the degree of the tilting

indicates variation in the amount rotation expressed in the degree of vertical displacement

along the main scarp.

The head zone is also characterized by numerous fractures and tension cracks.

The fractures and tension cracks are mainly near the edges of the main scarps with few

are also found within the crown area. Their orientation is generally parallel to the main

scarps. On the west side of the head, the cracks are ~30-130 m long with ~1-7 m wide

opening while on the side are ~15-40 m long ~0.5-5 m opening. Some of the fractures

that are located around the end of the main scarp are oriented slightly perpendicular to the

main scarp. The increase in sizes, intensities and density of the extensional fractures from

west to east likely indicates an increase of the degree of stretching from east to west.

The material exposed in the main head scarp was identified in the orthophoto as

series of white-gray transitioned to the east into a more tan-brown, and tan-white-tones

(Figure 7a). Field checking confirms that the contacts between these difference tones are

associated with different lithologic contacts. Detailed mapping indicate that the white

gray tone is associated with light gray-basalt, the tan brown with red brown basalt, while

the tan-white tone associated with the upper conglomeratic sandstone (Figure 12, and

17a, and b). From the hand specimen description in the field, the altered light gray basalt

33

is vesicular-amygdaloidal-porphyritic texture with some vesicles filled by calcite. Few phenocrysts are evident: plagioclase (5 % < 3 mm) and olivine (7 % < 2 mm). The thickness of this unit is about ~ 5-8 meters. A thin layer of tuff is at the base of this unit. Below this unit is a thick altered red brown basalt, the color varies from reddish to dark brown. The structure is apparently massive but appears to have columnar jointing. This unit is composed of olivine (7% < 2 mm) and pyroxene (2 % < 2 mm) phenocrysts. The presence of the tuff layer between basalt units indicates that that the lava flows are from different eruptions. For this study, however, we mapped these units as series of upper light gray and red brown basalt flow unit as they are composed of more than basalt flowsheet that are hard to differentiate in the field (Figure 12 and 17). The upper conglomeratic sandstone is light-gray to red brown, poorly consolidated and friable and poorly sorted with cobble to fine gravel- sized clasts. The composition is of feldspar and lithic fragments with tuffaceous materials as the matrix. The clasts are mainly mafic igneous rocks with small amount of felsic rocks and quartzite. The thickness of this unit ranges between ~ 15 m - 20 m. A thin reddish color band is evident in the upper part of this unit, right below the light gray and red-brown basalt, suggesting a baked zone contact (Figure 17a).
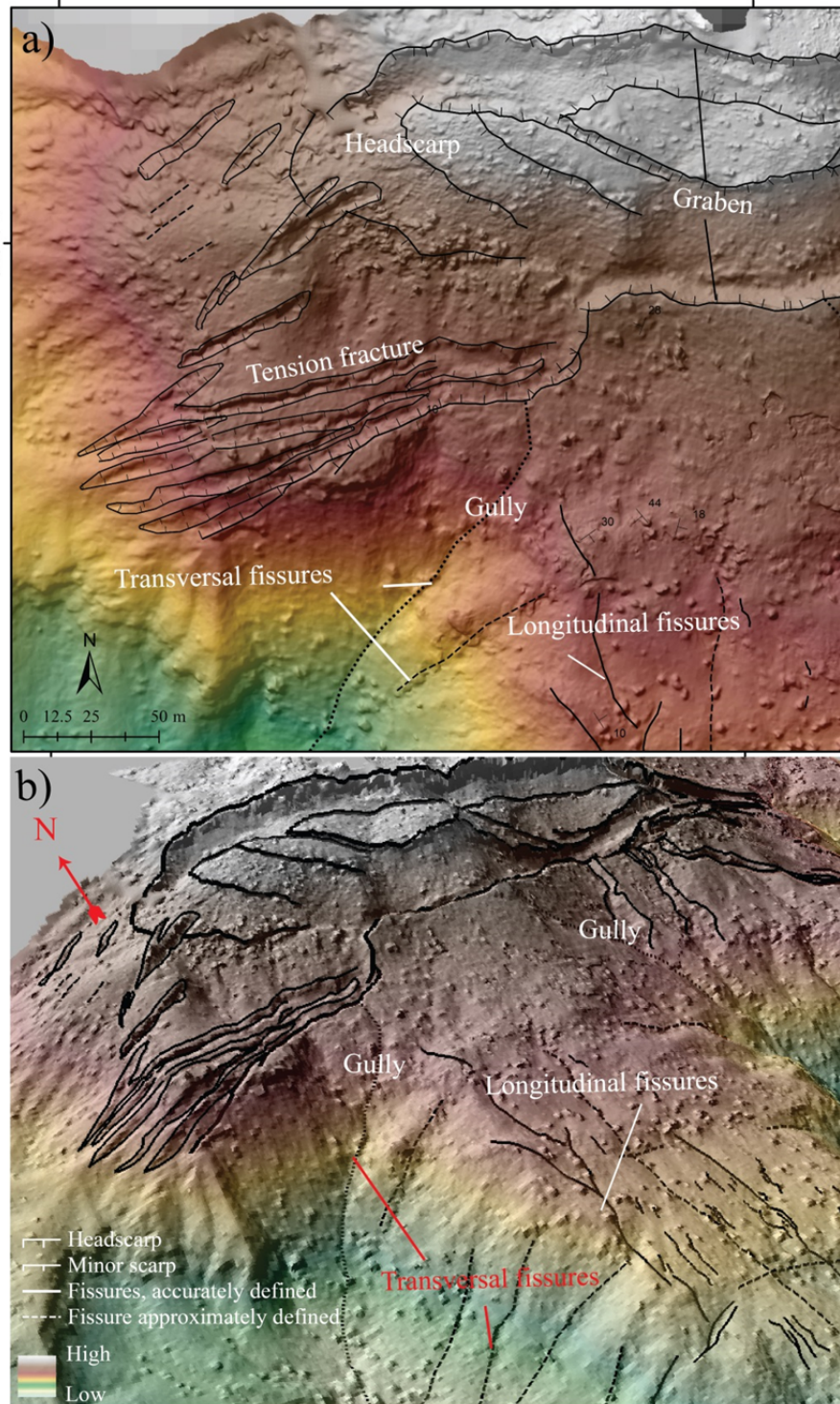
Figure 16. The map view (a) and oblique view (b) of the landslide features observed around the head and main lobe which includes head scarps, tension fractures such transversal and longitudinal fissures on the hillshade and DEM. Some gullies are also present at some hillslope.

35
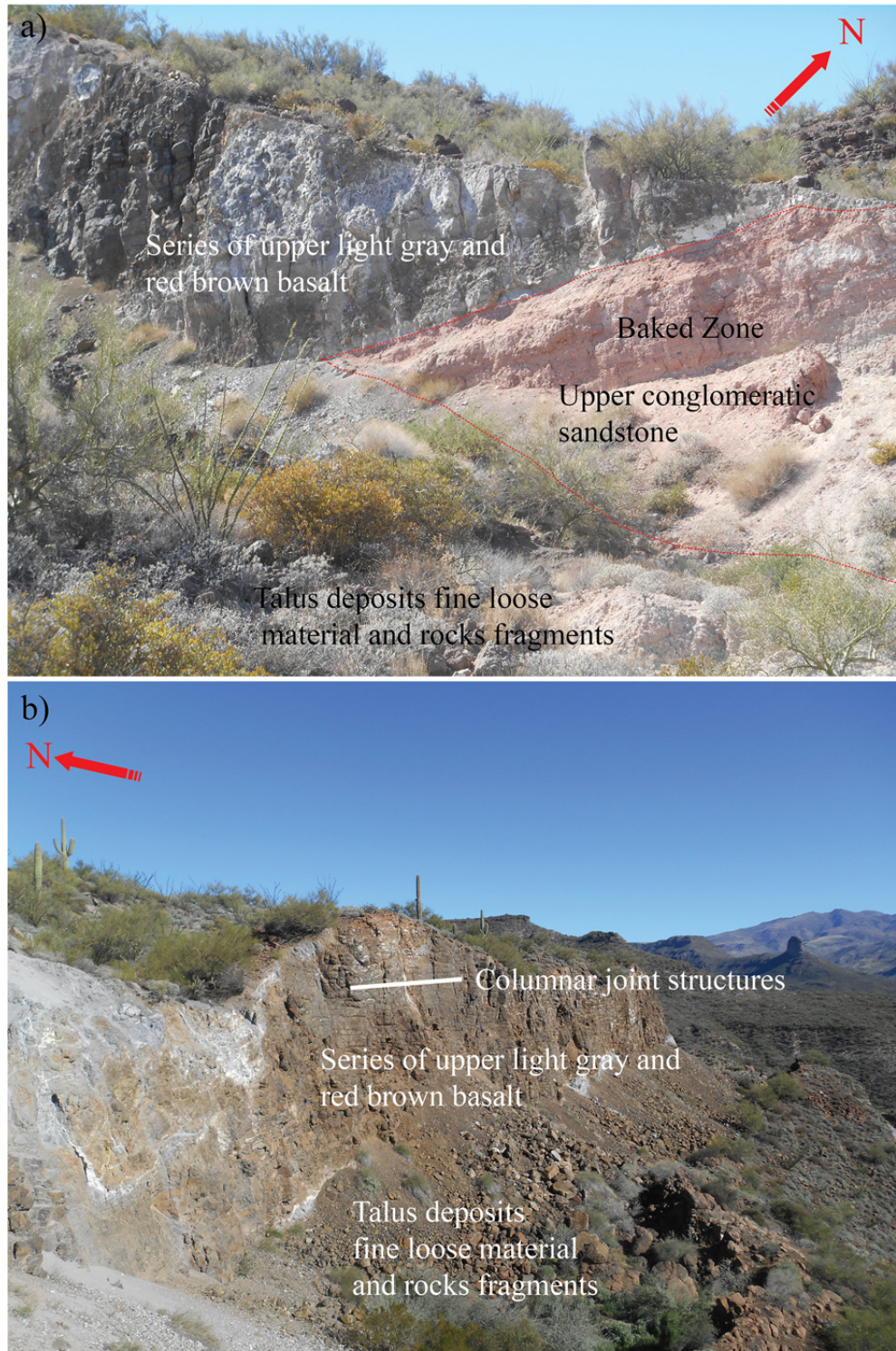
Figure 17. Field photographs of the Hickey Formation exposed along the main head scarp and head of BCC landslide. a) Series of upper light gray and red brown basalt overly the upper conglomeratic sandstone. Reddish band at upper part of the conglomeratic sandstone unit represents a baked zone contact between this sedimentary rock unit and

basalt flow. b) Series of basalt flow units that comprise of multiple basalt flowsheet: the red brown and light gray basalts. The red brown basalt shows a jointed structure while the light gray basalt has a vesicular and massive structure. Refer to Figure 15 for location.
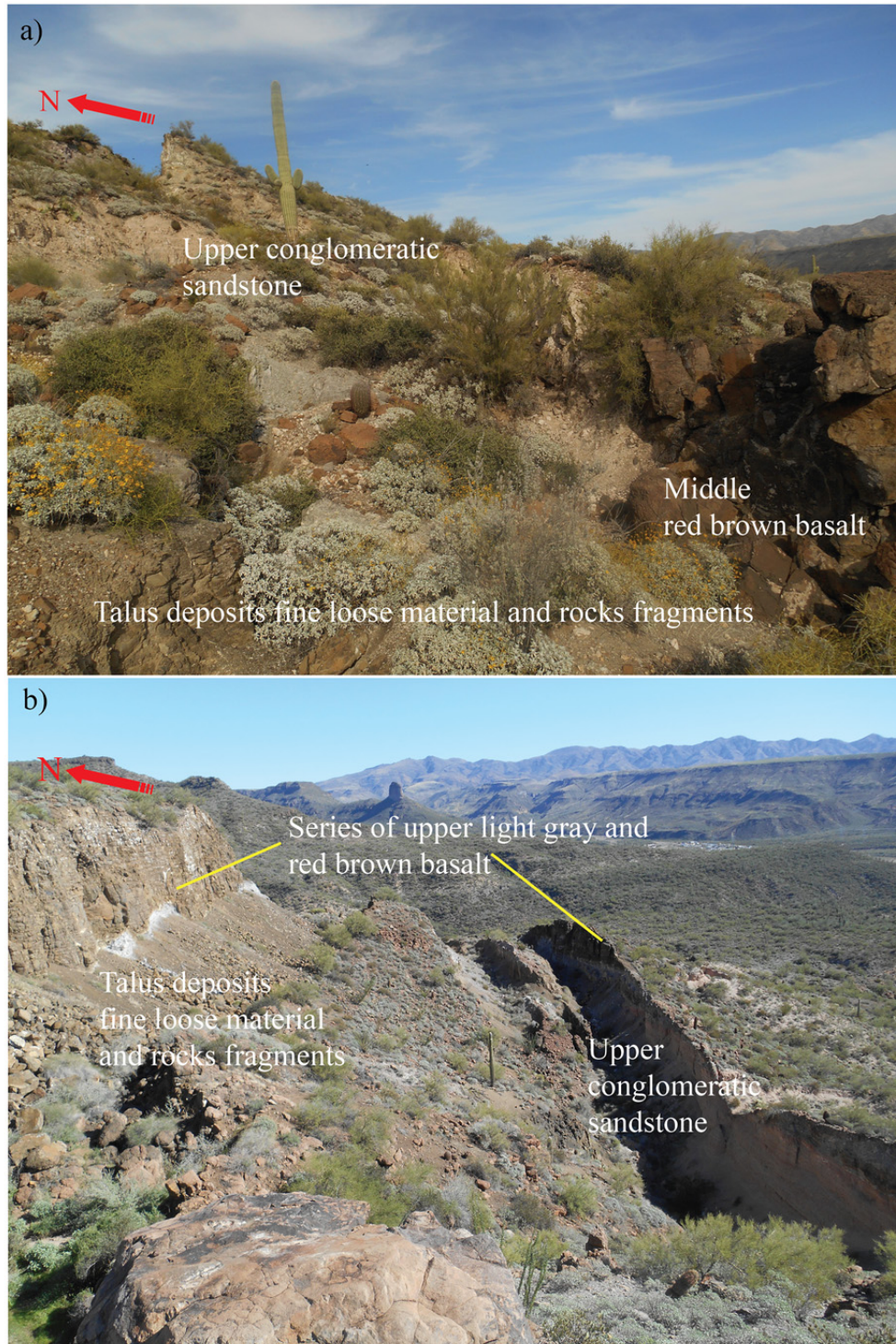
Figure 18. Field photographs of the series of upper light gray and red brown basalt, and upper conglomeratic sandstone unit exposed along the main head scarp and head of BCC landslide. a) The damage zone along the head scarp area. Contact between upper conglomeratic sandstone and the basalt is still observable along this region. b) Picture of newly formed open fracture with an opening of ~10m. Refer to Figure 15 for location.

We estimate the thickness of each layer using its spatial distribution, bedding and topographic profile extracted from the DEM. Because most of the layers are sub horizontal, the thickness can be easily estimated using the elevation difference of the contacts. The thickness of light gray and red brown basalt is ~ 42-46 m and the upper conglomeratic sandstone is ~ 10-14 m.

Along the base of the main scarp, a talus deposit accumulated. The talus is composed of fine loose material and rocks fragments fallen down from the main scarp. The debris pile is also observed along the minor scarp, where the material is coming from the uplifted blocks within the graben (Figure 18). We assigned these talus deposits as colluvial deposit in our local stratigraphic column (Figure 13).

Zone B: Main Lobe

The main lobe is located directly SW from the center of the head zone. The morphology of the main lobe is characterized by hummocky ridge-like features and is symmetric in plan-view (Figure 14) with general topographic slope of ~15 ° and local slopes of ~ 24˚ to 55˚ (Figure 15). The surface morphology is rough and is covered by sparse and moderate vegetation including bushes, Palo Verde and saguaro cacti and debris. Extensional fractures (longitudinal and transverse open cracks) dominate the structural configuration of this zone. North-trending lineaments are observed through the imagery, perpendicular to the trace of the main scarp, these lineaments are attributed to

longitudinal fissures as part of the NS extensional fracture system. Subtle lineaments parallel to the main scarp are observed in the orthophoto and in the hillshade and slope maps and are attributed to EW transversal fracture system. They are identifiable as a subtle topographic break in the topographic profile. Our new high resolution topography data has significantly improved the observation and interpretation of the landslide features as these subtle features were not visible in the lower resolution data. Small scale compressional features are also observed. Rills and gullies are also developed along the outer edges of the lobe where the slope is quite steep.

The dimensions of the longitudinal cracks vary from ~0.75 - 68 m with opening of ~0.22-1.2 m. Small scale tension cracks (< 0.75 m long with opening of ~0.02-0.2 m) that are perpendicular to the main scarp are identified in the field, but not visible in the imagery (Figure 19 and 20). The open fissures and cracks are filled in many places by calcium carbonate (caliche) indicating intensive leaching processes happen along fissures. These cracks (both longitudinal and transverse) are distributed all over the active lobe but mostly on the west side. The intensity of the fracturing is relatively lower on the east side and on the uppermost part of the lobe where the surface is mostly covered by debris material. The transverse fractures are expressed in the imagery as tearing surface and curved lineaments and are mostly located at the lower base of the west side. The absence of the transverse cracks at the east side of the slide may indicate different rate of extension between the east and west side. Indication of a slight counterclockwise rotational motion is evident at the west side of the slide area.

Some of the transverse cracks have been incised by ~0.4-1 m deep gullies and are filled by debris from above. The vertical and lateral displacement of the layer across the

gullies support the claim that the gullies are incised extensional features and not simply a result of hillslope processes only. The E-W trending gullies are distributed along the steeply slope area around the edges of the lobe, extend down to the base of the slope and eventually joining the main stream.

At the southern end of the lobe, near the foot area, compressional features are observed. These shortening features are including transverse ridges, topographic rise and toe (Figure 21). The transverse ridges are indicated by curve lineaments or bends, this feature is expressed as a convex break of slope in the morphology map (Figure 14). Notably, some plants are grown on a rotated surface and it is localized in areas with "popcorn" weathering patterns indicating significant clay in the underlying sedimentary layers at this level.

The middle red brown basalt unit found along toe area originated from the upper hill and has been disturbed and transported to its present position. The unit is tilted to the north and emplaced above the lower conglomeratic sandstone, indicating an earlier phase of slumping and backward rotation (Figure 22a). The pumiceous sandstone unit at the base of the main lobe dips gently uphill (Figure 22b). This unit is exposed because the material at the edge of the toe was eroded by the active channel. The toe of the main lobe is represented in the topography as a bulge in the topography created as material mounds up at the end of the lobe. The toe is characterized by convex break of slope with a curve-shaped lineament that is parallel to the contour in the morphology map (Figure 14). The boundary of the toe however, continues onto the SE lobe with the bulging and topographic rise that may indicate southward directed thrust faulting (Figure 21).

Figure 19. Photographs of open fractures and cracks found along the main lobe. a) Longitudinal crack at the lower conglomeratic sandstone show a 0.3 m opening and 0.05m vertical displacement, b) Longitudinal cracks at lower conglomeratic sandstone with 0.5 m vertical and 0.3 m horizontal displacements. Refer to Figure 15 for location.

Figure 20. Photographs of open fractures and cracks found along the main lobe. a) Longitudinal cracks at lower conglomeratic sandstone with 0.6 m vertical and 0.7 m horizontal displacements; the surface of the lower conglomeratic sandstone is covered by caliche. b) Small longitudinal cracks across the main body with 0.05 m vertical and 0.1 m horizontal displacements. Refer to Figure 15 for location.

The materials exposed across the main lobe consist of mostly thick lower conglomeratic sandstone, clayey sandstone, and slope wash materials, which consist of series red brown basalt and light gray basalt fragments from the upper slope, and middle red brown basalt unit. The contacts between these units however are not clearly visible from the imagery. Field-checking was necessary to accurately locate the lithologic contacts. In the field, the lower conglomeratic sandstone is tan-gray colored, unconsolidated and friable and is poorly sorted. The texture is matrix supported with sub-angular to sub-rounded clasts up to 70 cm in diameter. The matrix consists of coarse-sand sized feldspar, lithic fragments, and tuffaceous materials. The clasts are felsic and mafic granitoid rock fragments (35%), basaltic-andesitic rock fragments (55%), and quartzite, chalcedony, and meta-volcanic rocks (15%). The NE dipping layer (N290E/32NE) show a coarsening upward graded bedding structure (Figure 23a and b). The thicknesses of this layer range between ~ 42 - 46 m.
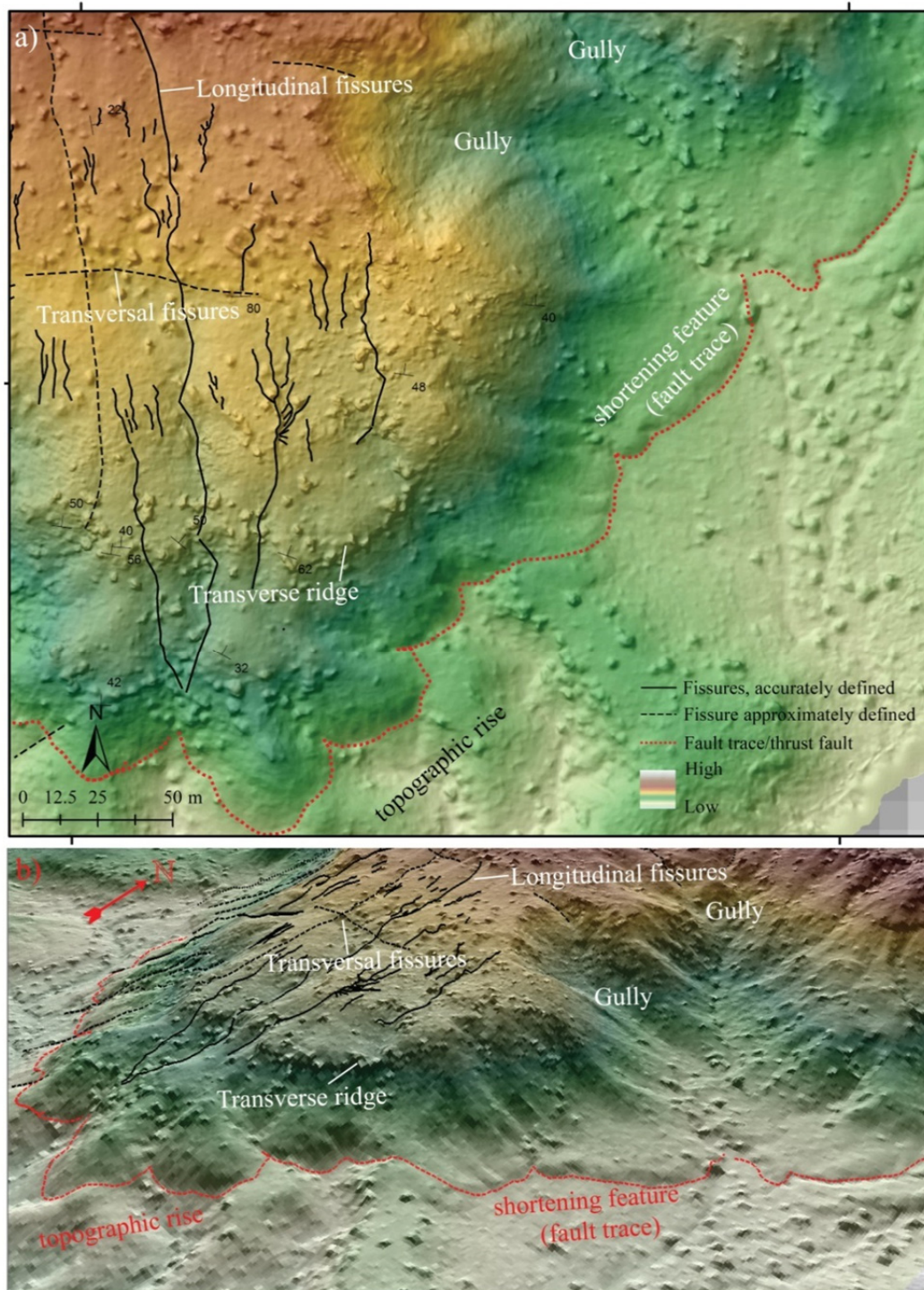
Figure 21. The map view (a) and oblique view (b) of the landslide features observed at the toe which includes shortening features, topographic rise, transversal and longitudinal fissures and transverse ridge on the hillshade and DEM. Debris materials are distributed randomly on the crest of the lobe. Some debris fragments create a continuous curve-shaped feature near the foot of the slide.

44

Figure 22. Field photo of outcrops observed across the main lobe body, a) The middle red brown basalt detach to the lower conglomeratic sandstone, b) outcrop of an interbedded pumiceous sandstone at base of west side of the landslide within the clayey sandstone unit. Refer to Figure 15 for location.
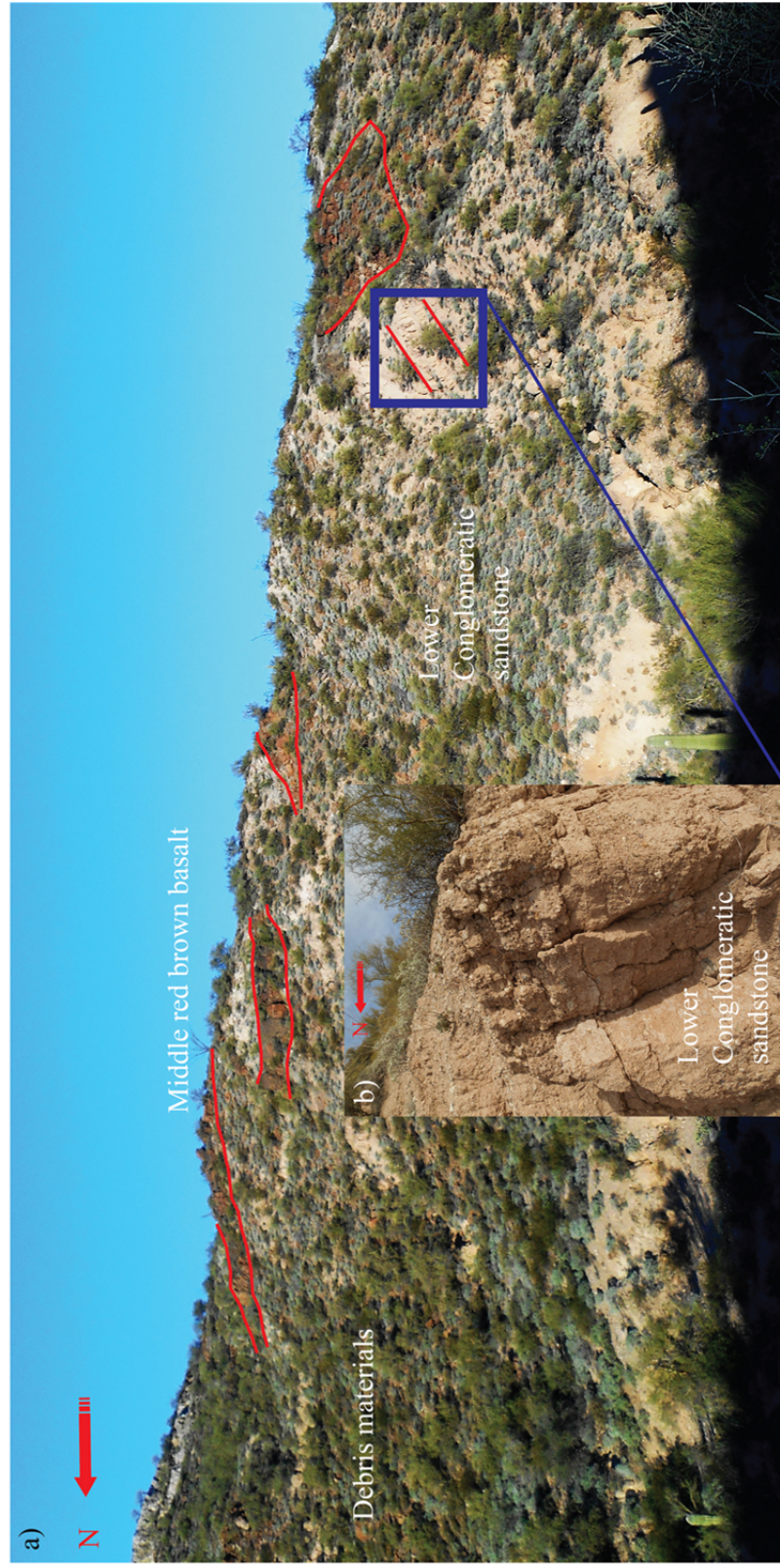
Figure 23. (a) photo show the general overview of the hillslope within the main lobe body, showing the alignments of middle red brown basalt units (red lines). (b) detailed photo of the material forming the hillslope which mostly consist of thick lower conglomeratic sandstone. Camera facing to the east. Refer to Figure 15 for location.
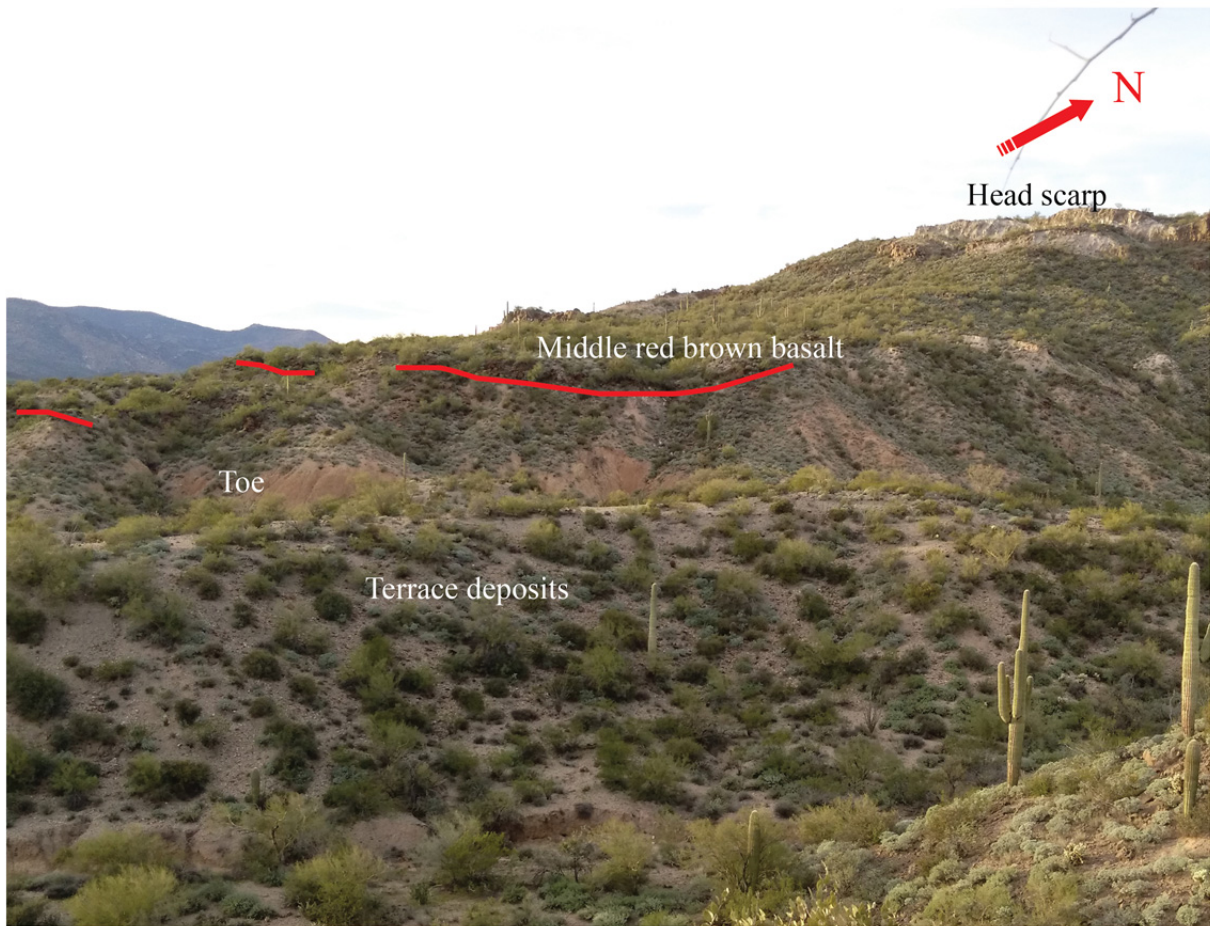
Figure 24. Field photo of a layer of middle red brown basalt covered the hillslope of main lobe, which is indicated by a red line. Outcrops forming hillslope consist of thick lower conglomeratic sandstone; this conglomeratic sandstone dips north, N290E/32NE (e). Refer to Figure 15 for location.

The tan brown clayey sandstone unit is exposed below the lower conglomeratic sandstone near the toe of the main lobe (Figure 24). The unit is unconsolidated and moderately-sorted with a very fine to medium grain size. The material is composed of unconsolidated calcareous material, quartz, feldspar, and clay materials. At the base of this unit is a 20 cm thick interbedded pumiceous sandstone that composed of well-sorted pumice, tuff and lithic of altered volcanic clasts. The bedding of this interbedded layer is

oriented at N292E/10˚ NE. Field test on the hand sample indicate that the unit has good porosity (Figure 22b). This thinly bedded layer is thought to be the slip surface of the landslide due to the abundance of clay in the contact zone.

Zone C: Southeast Lobe

The Southeast (SE) lobe is located on the eastern side of the landslide, below the minor scarp. It appears in the morphology as irregular ridges (Figure 14 and 25). The roughness of the surface and the amount and type of vegetation cover is similar to the other zones. In this zone, the landslide material is moving as a block. As it is displaced downslope, it maintains its coherence and is clearly defined in the mapping.

In this region, NW-SE trending fracture lineaments are observed throughout the lobe, and series small scale range of NW-SE of en-echelon fractures were also observed along the eastern section. The intensity of the fractures in this zone is relatively lower in comparison to the main lobe zone, but the damaged zone is larger, particularly at the southeastern edge of the margin of the SE landslide zone (Figure 26). The fractures are parallel to the minor scarp trending (Figure 25 and 27a). The less intense fracturing may indicate that the deformation along the main lobe region is higher than in this zone. The extensional fractures are closely-spaced, stepping and are oblique to the main scarp. The NW-SE lineament is likely longitudinal fissures. The fractures are ~1.5 – 5.5 m wide and ~70 - 85 m long. They are represented in the landscape as a complex of concave-convex change of slopes.

The current width of the open fractures does not represent the original width of the tension fractures. Hillslope processes have modified the features and obscure their

original geometry. The presence of the longitudinal fissures in this zone indicates that this area is still influenced by the landslide but is not as intensely deformed as the main lobe zone.

The distribution of the materials exposed along the SE lobe is easily identified on the orthophoto as red brown that transitioned to the north gradually from white-gray to light-gray greenish, to red-brown-greenish, white brown and dark brown colored tones (Figure 7a). The field checking confirms that the boundaries between these differences tones are associated with different lithology contacts. Detailed mapping shows that the red brown tones on the orthophotos are associated with lower conglomeratic sandstone and clayey sandstone unit, while the white-gray is upper conglomeratic sandstone, the light gray greenish tones is lower light gray greenish basalt, dark brown is associated with middle red brown basalt (Figure 28a and 29a), and light gray-dark brown tones is associated with series of upper light gray and red brown basalt (Figure 7a, 27a).

In general, the materials exposed across the SE lobe are similar to the main lobe, except for the presence of lower light gray greenish basalt emplaced between the lower conglomeratic sandstone (Figure 27b, 28b, and 29b) and clayey sandstone unit in the SE lobe zone (Figure 24b). The absence of this unit in the main lobe is possibly due to the irregularity of the basalt emplacement along the pre-existing topography. There are no indications that the lower light gray greenish basalt material has been displaced across the main lobe body although there is a possibility that it was displaced but is covered by debris materials (see Figure 30 for detailed reconstruction of geologic profile develop in this area). The lower light gray greenish basalt is vesicular-amygdaloidal-porphyritic texture (< 20 %) with some vesicles filled by olivine and calcite, consist of altered

49

orange-brown olivine (< 7 %, < 5 mm) and plagioclase (< 3 %, < 3 mm) phenocrists in very fine grained of greenish gray groundmass of minerals. In this region, this unit appears to dipping to the north-nortwest and generally covered the east-southeastern part of the mesa.
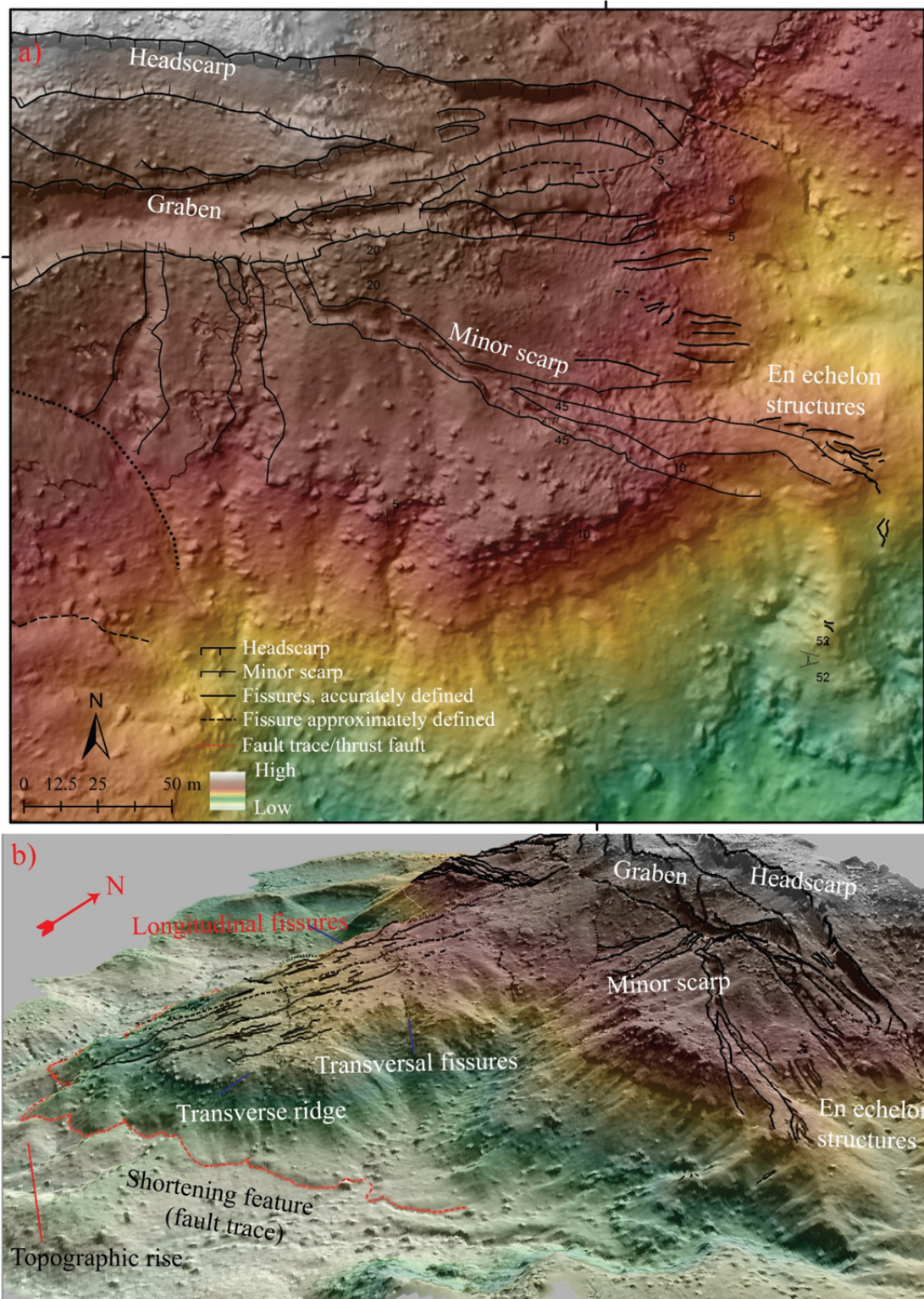
Figure 25. Indicate that a) is a map, and b) is the oblique view of the landslide features in the SE lobe on the hillshade and DEM map show minor NW-SW scarps, shearing, and intensive fissures at the edge of the east side margin of the SE lobe.

Figure 26. Photographs of features observed along the SE lobe body. a) Damage zone at surface of the lower conglomeratic sandstone unit at the eastern edge of the slide of the SE lobe body. This unit has been displaced 0.25 m vertically and 0.6 m horizontally. b) Minor scarp with 1.5 m vertical displacement at red brown basaltic-andesite unit with intensive platy jointed structure. Refer to Figure 15 for location.

Figure 27. Photographs of features observed along the SE lobe body. a) Contact between the upper conglomeratic sandstone and series of upper light gray and red brown basalt with reddish color at the contact (baked zone). b) Small transverse cracks at the lower

light gray greenish basalt with 0.04m vertical and 0.07m horizontal displacements. Refer to Figure 15 for location.

Figure 28. Photographs showing some of the units exposed across the SE lobe. (a) show the middle red brown basalt contact with the lower conglomeratic sandstone unit, and (b)

show the lower light gray greenish basalt with vesicular-amygdaloidal structure contact with lower conglomeratic sandstone. Refer to Figure 15 for location.

Figure 29. Photographs showing view of upper conglomeratic sandstone contact with the middle red brown basalt (a), and the lower light gray greenish basalt contact with lower conglomeratic sandstone. The distribution of the basalt unit are discontinue to the landslide. Refer to Figure 15 for location.
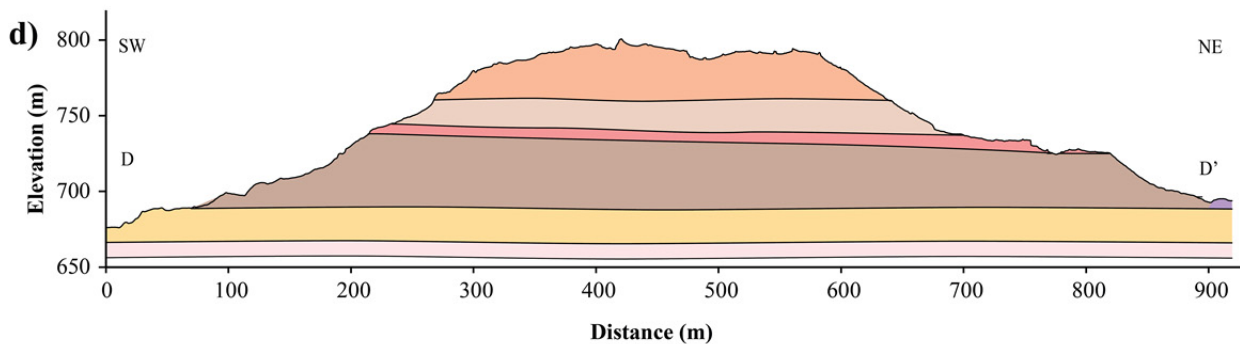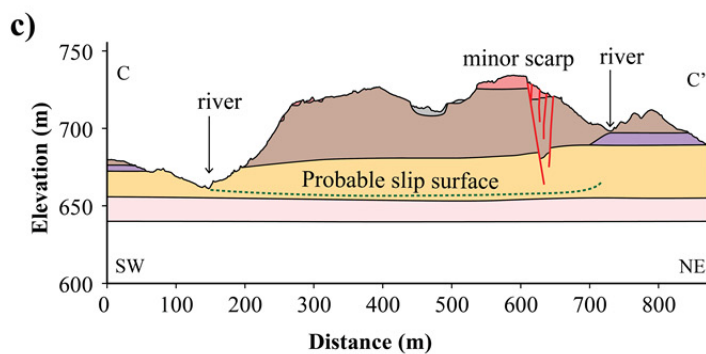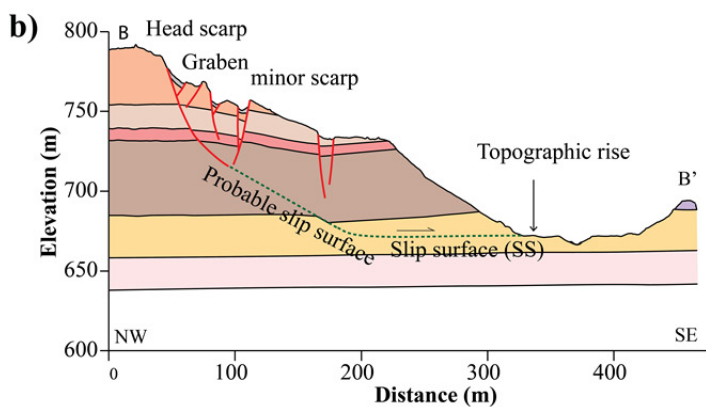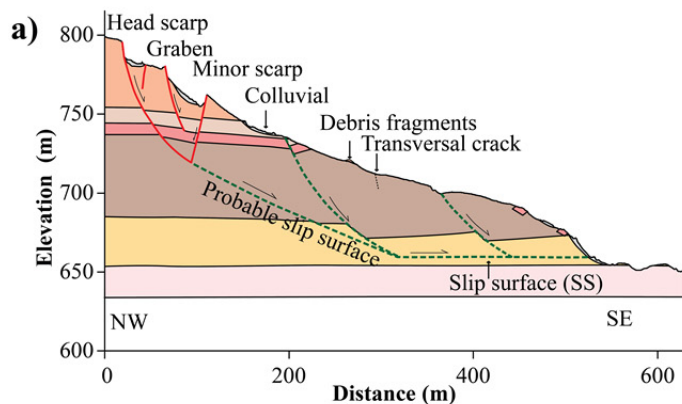
Figure 30. Geologic profiles through the slide and related areas (see Figure 7a for location of the profile lines). The topography are extracted from the 20 cm DEM. (a) and (b) cross sections pass through the entire sections of head, main body and toe, show the interpreted interior geometry of the main lobe and a possible slip surface. The suggested slip surface is indicated by green color represents at least two slide events occurred in this region. (c) Profile across the main body dissecting region of main lobe and oriented perpendicular to the main landslide direction. (d) Cross section along the crown displaying the original thickness and geometry of the stratigraphy prior to the landslide.

The fissures are not well-developed in the SE lobe, but the northwest-southeast long lineament that has ~1-5 m – 4.5 m wide separating the SE lobe body into two parts. In the northeast, the units are tilted to the south (represented by red brown basalt of strike and dip measurement N 80 E/20˚S). In the southwest portion, the units are slightly tilted to the north (represented by red brown basalt of strike and dip measurement N 230 E/10˚N).

Surface Displacement

We calculate the surface displacement rate by calculating the difference of original and present coordinates of the 17 survey stations deployed since 1998. The original survey was conducted using total station with a local reference station while the 2016 measurement was conducted using differential GPS that automatically records the position in a global coordinate system. We transform the data from the first measurement into global coordinate system to be able to compare the two datasets using simple transformation on Cartesian plane system with the position of instrument station as the reference point (considered as a stable point). This station was located outside of the landslide area and was surveyed using handheld GPS (1998). The result of the transformation is presented in Table 5.

57

In this analysis we assume that the instrument station and BM 1 benchmark is not moving. We then calculate the changes of the position of all points from the 1998 in comparison to the 2016 survey. For the vertical transformation, we first average the differences between the elevation of the instrument station and BM1 and use the average value to adjust the elevations of all other stations. We got the difference elevation of BM1 at -352.884 m and the difference of instrument station at -352.782 m with the average of -352.833 m and apply them to put the 1998 survey points into 2016 coordinate system. The horizontal transformation is then calculated by translating the 1998 and 2016 dataset into 0,0 and rotate around instrument station and BM 1. We generate the degree of rotation of ~29˚ at BM 1 and 0.000038˚ at the instrument station. It appears that the magnitude of the rotation around the BM 1 is too high, but the rotation around the instrument station is within our expected range. Assuming that the position of the instrument station is stable over time, we apply the coordinate of the instrument station from the 2016 into the 1998 data and generate global coordinate system for the other points. Results of the transformation are presented in Table 5 and show unacceptable discrepancies in the magnitude of deformation (-EW and NS components), except for the instrument station which is about -2.5 m EW, -0.29m NW and -2.5m of vertically (Table 5). Based on the field observations, we expect the magnitude of deformation to be <1 m. The elevation component of the calculation however, shows an acceptable value at -4.3 to -60 cm (Table 5). These surface displacement results should compare to the other measures of deformation that we compute. The dGPS data from the 2016 survey requires a minimum of 7 satellites to determine the location of the base station and is strengthened

by calculating its differential with the mobile station, resolving in mm-accuracy, much higher and reliable than the total station data.

The first transformation approach provides a significantly larger deformation value than we expected (see Table 5 for details), so we test another approach. The second approach is simpler. We estimate the displacement by calculating the differences in distance of each survey point (from the 1998, 2000, 2002, 2006 measurements) relative to the 2016 survey point of station 1 (BM1) only (see Table 6, 7, 8 and 9 for detailed calculation, and Table 10 for the average distance occurred from 1998 to 2016). We assume that the BM1 which is located south of the landslide toe is stable. The measurement of change in distance of the stations shows that all of them moved closer to BM1 during this time period (Figure 31). While all of the other stations appear to move closer to the BM1, the distance of the BM1 to the instrument station is increased by 0.89 m. This number could indicate that either the instrument station is moved westward toward BM 1 or that there is an error in the measurement of the positions. The error probably due to an incorrect in determining the instrument station during the measurement in 2016, because the location of instrument station has been relocated from its original position and was relocated using 1998 survey data. We roughly estimate a distance change of 0.55 to 3.6 m during this time period. Although the range is pretty wide, it is clear that all but one (BM 25) of the line length changes (absolute value) are greater than a meter. Even station 18, which look to be on a stable upper portion of the slide moved towards BM1 2.21 m—possibly indicating growth of the slide to the north (since 1998). Thus about a meter of horizontal motion has occurred over the past 18 years, yielding an approximate rate of ~10-60 m/yr motion.

59

Table 5. Transformation of the 1998 survey data and calculation of displacement relative to the 2016 dataset (the coordinate system is WGS84 UTM zone12. Blue shaded row indicate anomalously large displacement, indicating a large error in the data and/or calculation.

Number	Benchmark Point number	Total Station Measurement (1998)											dfGPS Measurement (2016)					dE between 2016 to 1998	dN between 2016 to 1998	dH between 2016 to 1998	Diplacement
		Bearing from Inst. Sta.	E1998	N1998	H1998	ΔE1998	ΔN1998	ΔH1998	α	East (E)	North (E)	Elevation (H)	East (E)	North (N)	Elevation (H)	ΔE2016	ΔN2016				
1	1	290.493	780.436	1091.527	973.373	-219.564	91.527	-26.627	20.493	395566.910	3772673.044	620.591	395553.93	3772645.751	620.489	-229.963	64.206	-12.982	-27.293	-0.102	30.22
2	2	304.202	755.114	1156.147	973.313	-244.886	156.147	-26.687	34.202	395541.588	3772737.664	620.531	395521.27	3772704.669	620.488	-262.619	123.123	-20.316	-32.995	-0.043	38.75
3	5	309.523	770.257	1197.510	981.346	-229.743	197.510	-18.654	39.523	395556.731	3772779.027	628.564	395529.50	3772747.608	628.488	-254.393	166.062	-27.233	-31.420	-0.076	41.58
4	8	320.291	760.597	1229.816	993.812	-239.403	229.816	-6.188	50.291	395547.071	3772811.333	641.030	395517.02	3772778.577	640.953	-266.875	197.031	-30.055	-32.757	-0.077	44.46
5	25	324.454	703.346	1270.213	1001.185	-296.654	270.213	1.185	54.454	395489.820	3772851.750	648.403	395455.86	3772813.19	648.309	-328.034	231.644	-33.963	-38.540	-0.094	51.37
7	18	335.998	837.576	1732.601	1109.790	-162.424	732.601	109.790	65.998	395624.050	3773314.118	757.008	395532.89	3773286.773	756.957	-251.002	705.227	-91.161	-27.345	-0.051	95.17
8	27	327.088	673.792	1417.704	1024.806	-326.208	417.704	24.806	57.088	395460.266	3772999.221	672.024	395408.72	3772955.445	671.925	-375.173	373.899	-51.548	-43.776	-0.099	67.63
9	10	335.176	770.261	1415.727	1026.963	-229.739	415.727	26.963	65.176	395556.735	3772997.244	674.181	395503.66	3772963.597	674.103	-280.233	382.051	-53.077	-33.647	-0.078	62.84
10	19	292.244	807.693	1408.992	1026.788	-192.307	408.992	26.788	22.244	395594.167	3772990.509	674.006	395536.93	3772960.123	673.38	-246.964	378.577	-57.240	-30.386	-0.626	64.81
11	Instrument station	0.000	1000	1000	1000	0	0	352.782	0	395786.474	3772581.517	647.218	395783.89	3772581.546	647.218	0.000	0.000	-2.583	0.029	0.000	2.58

60

Table 6. Change in length position of the benchmarks computed relative to station 1 (BM1) from 1998 to 2016. All values are in meters.

Benchmark	1998 Total Station Data							2016 dGPS Data							Change in length from 2016 to 1998
	East	North	Elevation	ΔE	ΔN	ΔH	Length	East	North	Elevation	ΔE	ΔN	ΔH	Length	
1.00	780.44	1091.53	973.37	0.00	0.00	0.00	0.00	395553.93	3772645.75	620.49	0.00	0.00	0.00	0.00	0.00
2.00	755.11	1156.15	973.31	-25.32	64.62	-0.06	69.40	395521.27	3772704.67	620.49	-32.66	58.92	0.00	67.36	-2.04
5.00	770.26	1197.51	981.35	-10.18	105.98	7.97	106.77	395529.50	3772747.61	628.49	-24.43	101.86	8.00	105.05	-1.72
8.00	760.60	1229.82	993.81	-19.84	138.29	20.44	141.19	395517.02	3772778.58	640.95	-36.91	132.83	20.46	139.37	-1.82
25.00	703.35	1270.21	1001.19	-77.09	178.69	27.81	196.58	395455.86	3772813.19	648.31	-98.07	167.44	27.82	196.03	-0.55
18.00	837.58	1732.60	1109.79	57.14	641.07	136.42	657.91	395532.89	3773286.77	756.96	-21.04	641.02	136.47	655.72	-2.19
27.00	673.79	1417.70	1024.81	-106.64	326.18	51.43	347.00	395408.72	3772955.45	671.93	-145.21	309.69	51.44	345.89	-1.11
10.00	770.26	1415.73	1026.96	-10.18	324.20	53.59	328.76	395503.66	3772963.60	674.10	-50.27	317.85	53.61	326.23	-2.52
19.00	807.69	1408.99	1026.79	27.26	317.47	53.42	323.08	395536.93	3772960.12	673.38	-17.00	314.37	52.89	319.24	-3.84
Instrument station	1000.00	1000.00	1000.00	219.56	-91.53	26.63	239.36	395783.89	3772581.55	647.22	229.96	-64.21	26.73	240.25	0.89

61

Table 7. Change in length position of the benchmarks computed relative to station 1 (BM1) from 2000 to 2016. All values are in meters.

Benchmark	2000 Total Station Data							2016 dGPS Data							Change in length from 2016 to 2000
	East	North	Elevation	ΔE	ΔN	ΔH	Length	East	North	Elevation	ΔE	ΔN	ΔH	Length	
1.00	780.44	1091.51	973.36	0.00	0.00	0.00	0.00	395553.93	3772645.75	620.49	0.00	0.00	0.00	0.00	0.00
2.00	755.13	1156.13	973.33	-25.31	64.62	-0.03	69.40	395521.27	3772704.67	620.49	-32.66	58.92	0.00	67.36	-2.04
5.00	770.22	1197.49	981.35	-10.22	105.98	7.99	106.77	395529.50	3772747.61	628.49	-24.43	101.86	8.00	105.05	-1.72
8.00	760.56	1229.79	993.82	-19.88	138.29	20.46	141.20	395517.02	3772778.58	640.95	-36.91	132.83	20.46	139.37	-1.83
25.00	703.33	1270.18	1001.14	-77.11	178.67	27.78	196.57	395455.86	3772813.19	648.31	-98.07	167.44	27.82	196.03	-0.54
18.00	837.50	1732.65	1109.79	57.06	641.14	136.43	657.98	395532.89	3773286.77	756.96	-21.04	641.02	136.47	655.72	-2.25
27.00	673.74	1417.67	1024.79	-106.70	326.16	51.43	347.00	395408.72	3772955.45	671.93	-145.21	309.69	51.44	345.89	-1.11
10.00	770.23	1415.72	1026.95	-10.21	324.21	53.59	328.77	395503.66	3772963.60	674.10	-50.27	317.85	53.61	326.23	-2.53
19.00	807.66	1408.94	1026.78	27.22	317.43	53.42	323.04	395536.93	3772960.12	673.38	-17.00	314.37	52.89	319.24	-3.80
Instrument station	1000.00	1000.00	1000.00	219.56	-91.51	26.64	239.35	395783.89	3772581.55	647.22	229.96	-64.21	26.73	240.25	0.89

62

Table 8. Change in length position of the benchmarks computed relative to station 1 (BM1) from 2002 to 2016. All values are in meters.

Benchmark	2002 Total Station Data							2016 dGPS Data							Change in length from 2016 to 2002
	East	North	Elevation	ΔE1998	ΔN1998	ΔH	Length	East	North	Elevation	ΔE	ΔN	ΔH	Length	
1.00	777.18	1083.28	973.33	0.00	0.00	0.00	0.00	395553.93	3772645.75	620.49	0.00	0.00	0.00	0.00	0.00
2.00	749.50	1146.92	973.30	-27.68	63.64	-0.02	69.40	395521.27	3772704.67	620.49	-32.66	58.92	0.00	67.36	-2.04
5.00	763.05	1188.81	981.29	-14.13	105.53	7.97	106.77	395529.50	3772747.61	628.49	-24.43	101.86	8.00	105.05	-1.72
8.00	752.19	1220.75	993.77	-24.98	137.47	20.44	141.21	395517.02	3772778.58	640.95	-36.91	132.83	20.46	139.37	-1.84
25.00	693.47	1258.96	1001.13	-83.71	175.68	27.81	196.58	395455.86	3772813.19	648.31	-98.07	167.44	27.82	196.03	-0.55
18.00	-	-	-	-	-	-	-	395532.89	3773286.77	756.96	-21.04	641.02	136.47	655.72	-
27.00	658.40	1405.23	1024.75	-118.78	321.95	51.42	346.99	395408.72	3772955.45	671.93	-145.21	309.69	51.44	345.89	-1.09
10.00	754.95	1406.88	1026.91	-22.23	323.60	53.58	328.76	395503.66	3772963.60	674.10	-50.27	317.85	53.61	326.23	-2.52
19.00	792.59	1401.52	1026.73	15.42	318.24	53.41	323.06	395536.93	3772960.12	673.38	-17.00	314.37	52.89	319.24	-3.82
Instrument station	1000.00	1000.00	1000.00	222.82	-83.28	26.67	239.37	395783.89	3772581.55	647.22	229.96	-64.21	26.73	240.25	0.88

Table 9. Change in length position of the benchmarks computed relative to station 1 (BM1) from 2006 to 2016. All values are in meters.

Benchmark	2006 Total Station Data							2016 dGPS Data							Change in length from 2016 to 2006
	East	North	Elevation	ΔE	ΔN	ΔH	Length	East	North	Elevation	ΔE	ΔN	ΔH	Length	
1	777.20	1083.27	973.34	0.00	0.00	0.00	0.00	395553.93	3772645.75	620.49	0.00	0.00	0.00	0.00	0.00
2	749.56	1146.87	973.29	-27.64	63.60	-0.05	69.34	395521.27	3772704.67	620.49	-32.66	58.92	0.00	67.36	-1.98
5	763.07	1188.81	981.31	-14.13	105.54	7.97	106.78	395529.50	3772747.61	628.49	-24.43	101.86	8.00	105.05	-1.73
8	752.23	1220.72	993.77	-24.97	137.45	20.43	141.18	395517.02	3772778.58	640.95	-36.91	132.83	20.46	139.37	-1.81
25	693.51	1258.95	1001.14	-83.69	175.68	27.80	196.57	395455.86	3772813.19	648.31	-98.07	167.44	27.82	196.03	-0.54
18	810.43	1726.04	1109.72	33.24	642.77	136.39	657.92	395532.89	3773286.77	756.96	-21.04	641.02	136.47	655.72	-2.19
27	658.49	1405.18	1024.73	-118.71	321.90	51.39	346.92	395408.72	3772955.45	671.93	-145.21	309.69	51.44	345.89	-1.03
10	754.99	1406.83	1026.92	-22.21	323.56	53.58	328.72	395503.66	3772963.60	674.10	-50.27	317.85	53.61	326.23	-2.48
19	792.61	1401.46	1026.74	15.41	318.19	53.40	323.01	395536.93	3772960.12	673.38	-17.00	314.37	52.89	319.24	-3.76
Instrument station	1000.00	1000.00	1000.00	222.80	-83.27	26.66	239.35	395783.89	3772581.55	647.22	229.96	-64.21	26.73	240.25	0.90

Table 10. Comparison of change in length position of the benchmarks computed relative to station 1 (BM1) from 1998, 2000, 2002, and 2006 to 2016. All values are in meters.

Benchmark	Δl 2016 to 1998	Δl 2016 to 2000	Δl 2016 to 2002	Δl 2016 to 2006	Average of change in length
1	0.00	0.00	0.00	0.00	0.00
2	-2.04	-2.04	-2.04	-1.98	-2.02
5	-1.72	-1.72	-1.72	-1.73	-1.72
8	-1.82	-1.83	-1.84	-1.81	-1.83
25	-0.55	-0.54	-0.55	-0.54	-0.55
18	-2.19	-2.25	-	-2.19	-2.21
27	-1.11	-1.11	-1.09	-1.03	-1.08
10	-2.52	-2.53	-2.52	-2.48	-2.52
19	-3.84	-3.80	-3.82	-3.76	-3.80
Instrument station	0.89	0.89	0.88	0.90	0.89

An unpublished dataset of InSAR calculation of the BCC landslide done by Jeffrey Moore of University of Utah for time period of 2011-2013 (personal communication) suggests that the BCC landslide is not active during period time (2012-2013) (see Figure 37 in the appendix A for details). However, InSAR data is better for characterizing vertical motion and hence the small amount of horizontal displacement (less than 60 mm/yr) with low vertical motion as indicated by this study might be too small to be captured within 2 years observation of the SAR data, or that the displacement occurred after 2013.

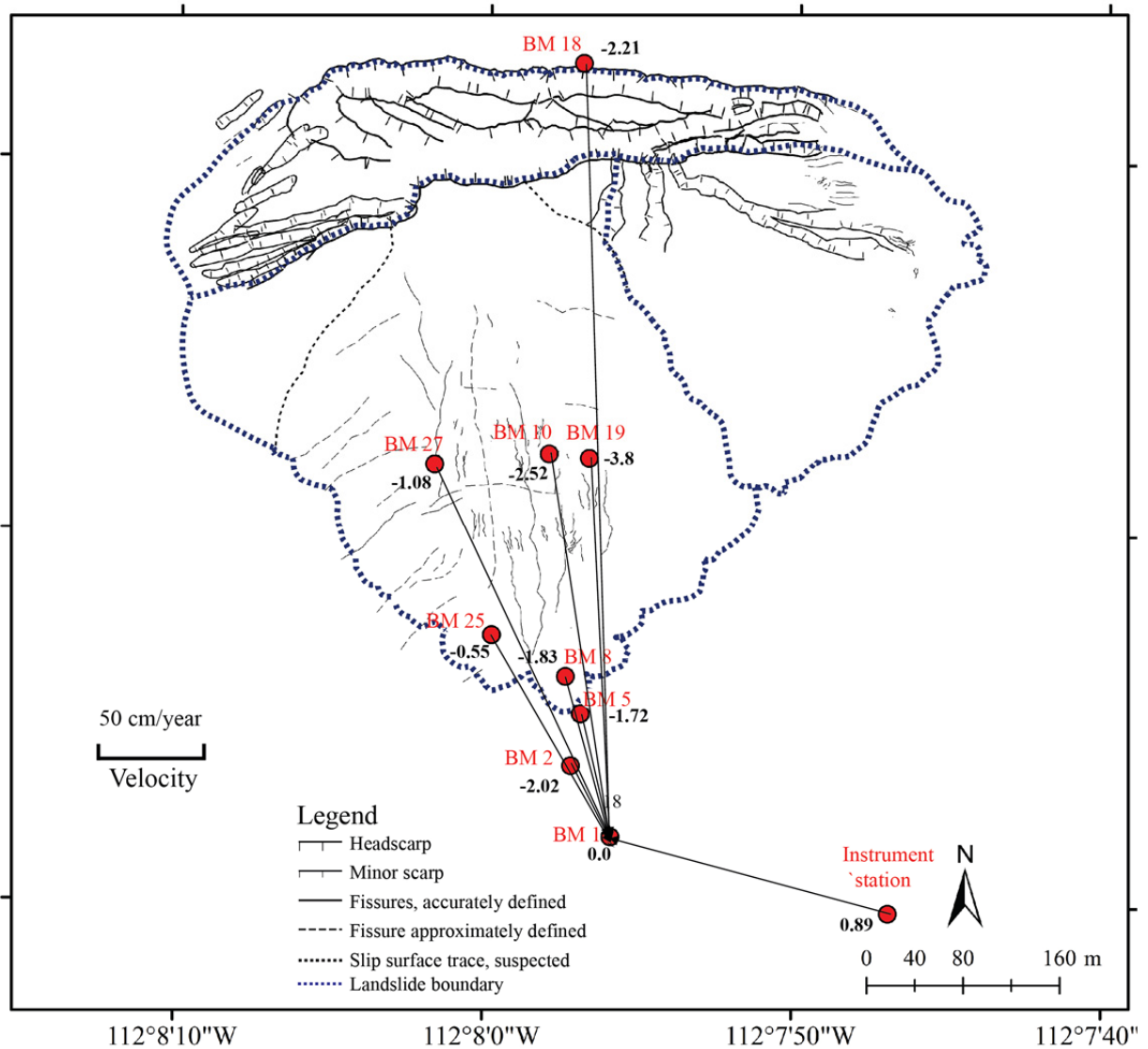Figure 31. Map showing average changes in distance of the benchmarks relative to station 1 (BM1), where the average is calculated from 1998, 2000, 2002,and 2006 survey data relative to 2016 measurement. Black arrow indicates the magnitude of the changes relative to station 1. Negative distance change means that the stations moved closer together. Changes shown here are 1998-2016. See also table 10.

CHAPTER 4

DISCUSSION

Geometry and Motion of the Landslide

The distribution and orientation of the disturbed ground surface of the landslide body provide significant information to the understanding of the sense of motion of the slide. Detailed geologic and morphologic mapping of the BCC landslide shows that the landslide body can be differentiated into three distinctive regions based on the deformation patterns: head, main lobe and SE lobe.

The sense of motion of the BCC landslide is varies spatially within the interior. The main trend of the extensional deformation along the main head scarp and the head of the slide is relatively east-west. The minor scarp are oriented slightly perpendicular to the direction of the main movement suggesting that the lateral component of the slide is moving relatively southward. The north-south longitudinal fissures along the main lobe indicate some spreading of the slide mass interior. These styles of structures suggest that there are different types of movement occurred between these regions. Also, the difference in the density and the size of the longitudinal fissures between the main and SE lobe indicate that these regions respond differently, possibly due to different magnitude of deformation as the block masses move downslope. The larger density and size of the cracks represent higher intensity of differential motion in the region.

The degree of stretching increases from east to west along the head. The degree of stretching can be intensified by preexisting fractures, decrease of rock strength, weathering, internal structures of the rocks, such as propagation of columnar joints in basalts, and contrast of lithology contact. Differences of overburden pressure, changes in

67

pore pressure and steepness of slope and slope shape also influence the degree of stretching along the head of the landslide. The difference in the extension rate also influences the slide motion along the major lobe/margin or SE lobe body beyond the head. The influence is expressed by a slight rotation of the main lobe near the toe to the southeast in respond to large discrepancies of the larger magnitude of lateral spreading between the east and west side of the body (Figure 12).

Topographic warps of irregular NE-SW trend along the emergent of the main and SE lobe of the toe provide a kinematic indicator of the slide. We interpret these features as thrust faults, formed in response to the block movement of the material from the head, pushing the material downward to the south and triggering thrust faulting near the end of its lateral spread (Figure 32b and c). The existence of the over-steepened slope and buckling or topographic rise at base and beyond the toe also indicate the southward movement of the slide.

The distributions of these features may reflect the geometry of the slip surface at depth. Based on profile reconstruction controlled by stratigraphic correlation, the slip surface of BCC landslide may evolve from a curve planar slip surface during the first slide event to more translational movement during the second landsliding event. The most prominent marker is the change of dip direction of the pumiceous sandstone at the base of the landslide. This inferred form of slip surfaces is also indicated by the existence of both normal and opposite-facing scarps along the main head, over-steepened slope as well as topographic rise and buckling at the base and beyond the toe (Figure 12 and 21). Indication of rotational slip surface is also observed by the presence of low angle dip of interbedded pumiceous sandstone at the base of the slide that is slightly tilted to the north

68

suggesting that the layer was disturbed by the slide motion (Figure 22b). The NW-SE trending minor scarp occurred across the SE lobe suggests that the extensional structures propagate outward to the east side accommodating the slide movement to the south.

Based on the detailed geologic and morphologic mapping and profile reconstruction, the elevation of the slip surface is estimated to be around ~656 m abs (Figure 30). The slip surface is occurred within the clayey sandstone unit which consists of silt, clay and very fine to coarse grained and interbedded pumiceous sandstone. The pumiceous sandstone layer within the clayey sandstone unit may be responsible for the slide as it creates an unstable bedding sequence.

It is challenging to determine the velocity of the BCC landslide because the age of landslide initiation is not well documented. Estimation of the surface displacement however is important to understand the landslide activity over time, to predict its future activity and to assess the hazards it posed to the surrounding area. The landslide is identified in the historical aerial photos taken in 1930 and 1980 (Figure 33a and b). We georeferenced these images in ArcMap and display them as layers for easy comparison. The comparison of the landslide geometry identified in these two aerial photos show similar gross features of the slide (see Figure 38 and 39 in the appendix A for detailed of the work done of georeferencing proceses). Visual inspection of these photos indicates that there are significant movements observed during this time period. The patterns show a varied displacement throughout the landslide body (Figure 33 c and d)). In particular, near the west side of the main lobe along the minor scarp where it shows a large displacement (21-25 m). The large displacement may be associated with the rotational of the main lobe as result of the second landslide event, where the head is collapsed through

translational slip surface, forming two steep cliff (normal fault) (Figure 35e). Based on this visual observation, we estimate the surface displacement is around 7-25 m over 68 years, resolving velocity of ~0.1-3.6 m/yr. However, this value may be not reflecting true displacement and could have been due to the error in the georeferencing process.

In addition to the rate velocity calculation, the presence of rill, gully and material deposits identified at the base of the toe indicate that surface process is dominant than the sliding. The hillslope process has reduced most of the steepness of the slope, causing the hillslope to become stable for long period time. The hillslope processes will subsequently diminish any indicators of landslide (i.e. debris material, rock avalanche, or earth flow generate from rocks basalt at the head). Despite the dramatic evidence of ground failure, especially in the head zone, the slide appears to be moving slowly. The occurrence of a disturbed ~35 years old Palo Verde tree (change the growth pattern from horizontal to vertical) within the SE lobe indicate that the landslide has been moving during the life span of the tree (Figure 32a). The relative magnitude of the displacement is by calculating the difference position of the established benchmarks measured in 1998 and 2016 (18 years) (Table 10, and Figure 31). Based on our calculation indicates that all of the stations on the slide moved closer to Benchmark 1 from 1998 to 2016 and suggest about a meter of motion of the slide over 18 years yields a very approximate rate of ~ 10-60 mm/yr motion.
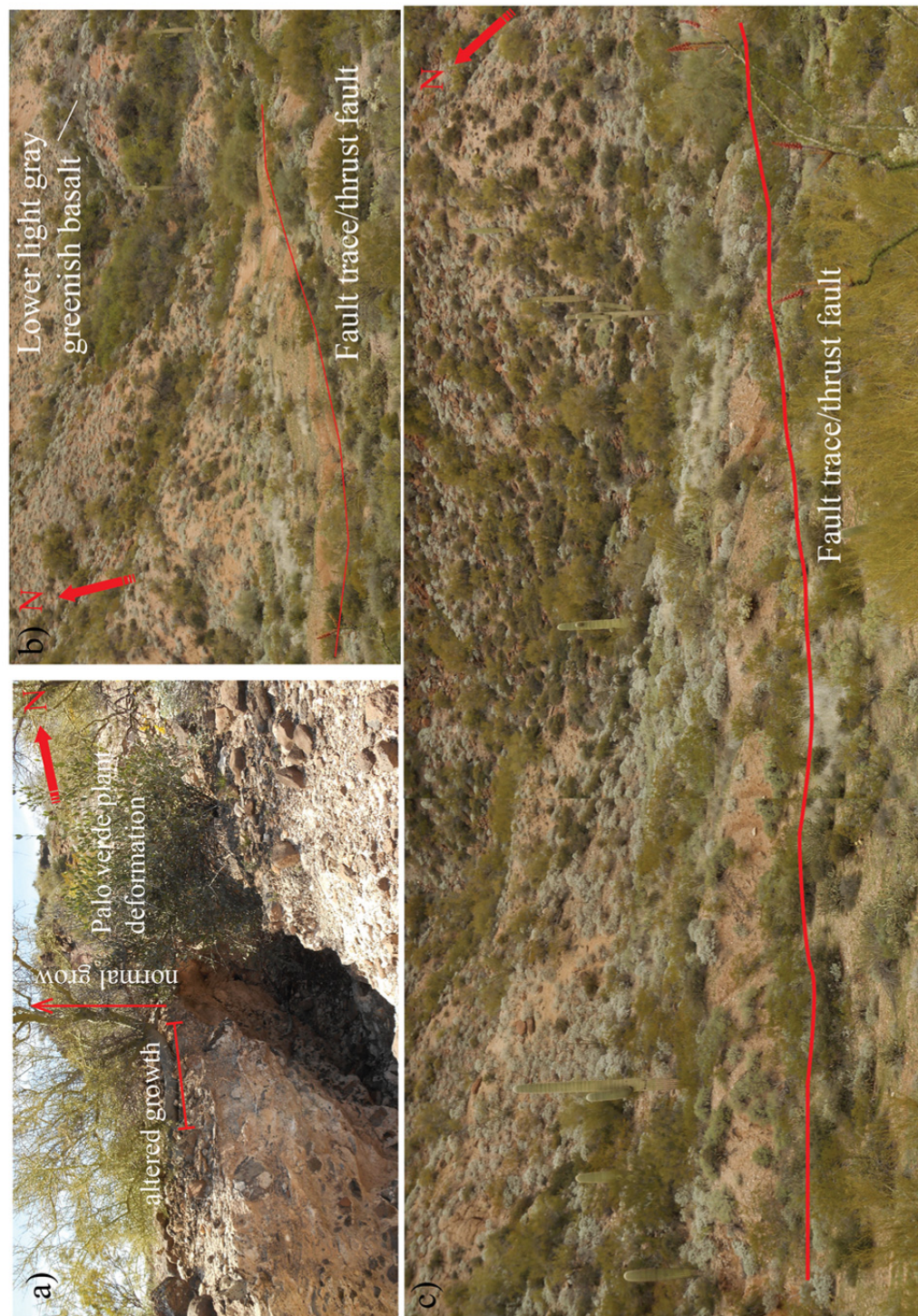
Figure 32. (a) Photographs of altered growth observed in a Palo Verde tree disturbed by the landslide. (b) Photograph of compressional feature (thrusts) observed at the main lobe body near the toe. See Figure 15 for location.

71
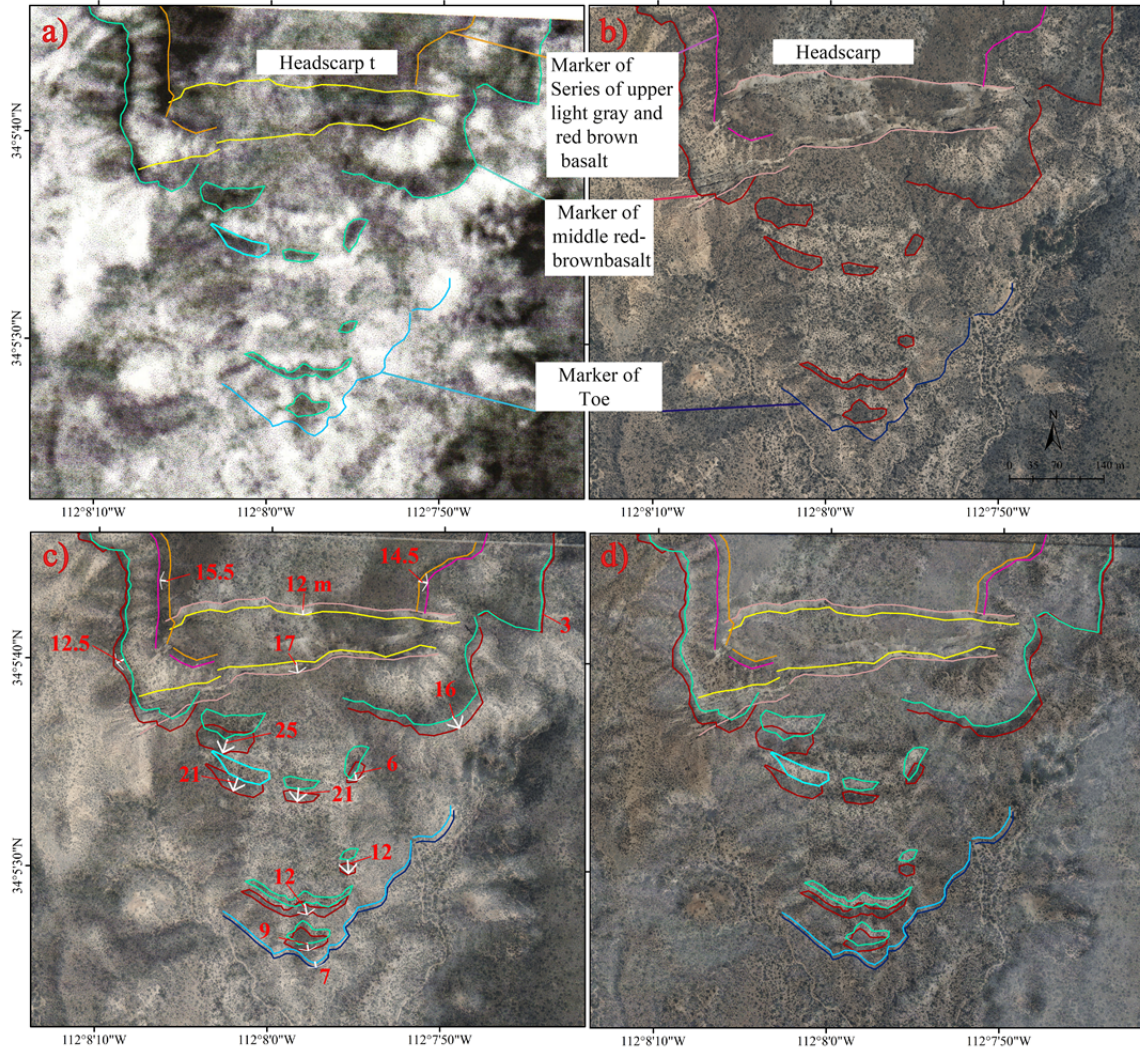
Figure 33. Comparison of landslide features identified in1930 (a) and 1998 (b) aerial photos showing a significant horizontal displacement. Similar geomorphic markers observed in both photos include: major and minor scarps, toes, and lithology contacts, represented by different line colors. In (a), yellow: scarps, light-blue: toes, orange: series of upper light gray and red-brown basalt boundary, and light green: middle red brown basalt boundary, in (b), light-pink: scarps, dark blue: toes, purple: series of upper light gray and red-brown basalt boundary, and red: middle red brown basalt boundary. I compare the features by superimposing both imageries. In (c), the 1998 aerial photo is set at 0% transparency and 1930 is at 50%. In (d), the 1998 is set at 0 % and 1930 at 50% transparency with RGB color was inverted from the previous one to highlight the contrast. Numbers indicate the amount of displacement in meter, the displacement is varies through the landslide region.

72

Factor Causing the Landslide

The BCC landslide involves originally horizontal layers of volcanic and sedimentary rocks units. Our mapping indicates that combination of factors including the geologic condition (rock composition, rock structures), morphologic (surface processes), hydrologic (stream incision) and weather conditions (seasonal storm events) altogether are the main cause of the landslide.

Two of the most prominent geologic factors of the slide are structures (joints and fissures) and the permeability of the rock units. The occurrence of intense fracturing like columnar joints in the basalt units as well as its vesicular structure provides a pathway for fluid to go through to the subsurface. The presence of the weathered and altered basalt, particularly along the joints, is evidence of invading fluid through the factures. The fluid will invade the permeable zone underneath the basalts (conglomeratic sandstone, clayey sandstone and pumiceous sandstone) and increase pore pressure as well as the weight of the rock mass. If this fluid reaches the impermeable zone (another basalt unit or clayey sandstone), this water will create a perched wet zone, possibly further decreasing the strength of the clay-rich materials at that level.

Another factor that may responsible for the initiation of the slide is the geomorphology, such as topographic gradient and slope shape. The steepest gradient of the study area ranges between ~28-52˚ and ~ 23-35 ˚ in the east and west side of the undisturbed zone. The steepest gradient in the main lobe is ~10-15˚ and local slopes of ~ 24˚ to 55˚ along the maximum stretch direction of the head of the slide. The occurrence of this steep topography may affect the slope stability at the margin. The shape of the slope also affects the slope stability, especially on how the surface and subsurface water

73

accumulate. The areas where steepest slope gradient along the east and west sides of the active lobe near the head of the landslide are considered as the most unstable region across the landslide area.

The BCC landslide is bounded by two prominent active streams on the east and west sides of the slide. Both of these active channel contribute to the material removal along the foot and toe in the east and west side of the slide during heavy storm. The lowering of the landscape along these bounding streams has diminished the lateral topographic support of the rock masses comprising the BCC landslide and thus most likely contributed to its motion.

The aforementioned factors may explain the movement in the active lobe. The structural block movement at the main head scarp was initiated by gravitational stresses, triggering the movement of materials below it. The occurrence of series of thick basalt flow and conglomeratic sandstone units at the top of the mesa combined with seasonal weather in this area increase the chance of structural block movement. During a winter (or summer) of sustained precipitation, the slide may charge with water, thus becoming heavier and possibly the basal interface weakens and so it moves. The precipitation in Arizona is highly depending on the altitude and period in year. The rain storm usually occurred during the monsoon season in early July through mid-September and sometimes between Novembers – March during the winter season. The summer storm was usually lasted more than one day causing more water infiltrate trough the tension cracks and internal structures of the basalts. This infiltration will increase weight and size of the underlying porous rocks below the basalt and combining together with the volume of the basalt adequately increasing the tensile stress. This high confining pressure of weight of

74

the overlying rocks and weakening the interface layer within the clayey sandstone cause the block mass subside down through the tension crack create two steeply dipping surface of failure at the upperpart of the slide. As the structural block downward, the lowest part beyond the head of the slide pushes laterally downslope through the slip surface.

Another possible factor triggering the landslide is earthquakes. Multiple earthquakes (M3.2, M4.0, and M3.6) were occurred on November 2nd, 2015. The epicenters are located ~7.2 km NE of Black Canyon City, Arizona, ~5 km from the BCC landslide. The sequence began with a M3.2 at 3:59 pm (foreshock) followed by M4.1 mainshock at 6.29 pm (located within 2 km of the foreshock). Another event, of M3.6 occurred 20 minutes later, located 4.2 km SSW from the main shock (see Figure 34 for the map of the earthquake epicenters). The BCC landslide is within the zone of MMI IV during the main shock, however our field observation indicate no disturbance and movement of the landslide in response to these earthquake events.

Figure 34. Map show the location of earthquakes epicenters of earthquakes occurred during November 2nd, 2015, near Black Canyon City, Arizona. The basemap is from the Google Earth imagery.

History of Movement

At least three periods of landslide movement may have occurred in the BCC

landslide with the clayey sandstone as the potential slip surface. The type of the landslide

movement is combination of translational and rotational movement. A schematic diagram

of the evolution of the landslide through time is presented in Figure 35. The topographic

profile for the diagram is generated from the present topography. There are several stages

of the landslide motion. At the first stage, the basalts are characterized by intensive

columnar joints and vesicular structures (Figure 35a). The joints then grow into open

fractures and propagate to the subsurface. During periods extended rainfall, the active

channel on the east and west side of the slide were filled with water, eroding the base of

76

the slide. The removal triggers the first southward slide along the curve-planar slip

surface at the basal surface (Figure 35b).

The processes repeated and the slip surface propagates backward (north) and

causing a subsequent translational and rotational movement along the main lobe and the

toe (Figure 35c). Due to the sliding, the middle basalt units then broke into several

distinct smaller blocks (red colored units) (Figure 35c). The slope is then stabilized and

surface processes are now dominant. The block mass of the middle basalt unit in the main

lobe is then transported downslope through hillslope processes (Figure 35d).

Intensive fracturing associated with 1st and 2nd sliding event increase the

impermeability of the layers and provides pathways for water to infiltrate the subsurface,

especially during heavy rainfall seasons. This infiltration cause the underlying

sedimentary rocks (conglomeratic sandstone, clayey sandstone and pumiceous sandstone)

to increase their weight and saturation. These changes and the high driving force from

series of the heavy overlying basalt unit unsupported to the south because of landscape

lowering promote collapse. These blocks move downward, forming two steep cliffs and

small graben at the head of the landslide and push the landslide body to the south. The

movement causes a small translational slide along the head and main lobe through planar

surface and the merge into the planar surface at the base of the slide (Figure 35e) and the

slope temporarily stabilized.

During the slope stabilization process, the base of the graben is filled with

weathered rocks and debris fragments came from above of the headwall, forming talus

deposits along the east-west of the graben. Furthermore, the block mass of basalt unit

along the main move further and spread downslope through slope wash, debris and other

77

hillslope processes reach the foot and the toe. During this movement, the slip surface propagates forward (Figure 35e). Other rainfalls during severe reactivated the slip surface and rotated the main lobe body and generate new slip surface along the foot area (3rd slip surface event). The slide move the body southward by translational (with slight rotational) movement as indicated by the tilted of the distinct part of basalt units to the north (Figure 35f). Due to the slope instability at the toe, slumping is occurred and moving another block mass of basalt and causing it to tilt to the north (Figure 35g). After this event, the landslide deformation rate is decreased and resumed to its present configuration (Figure 35h).
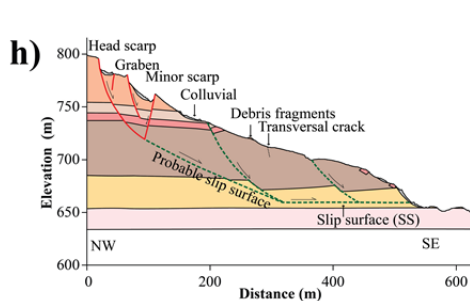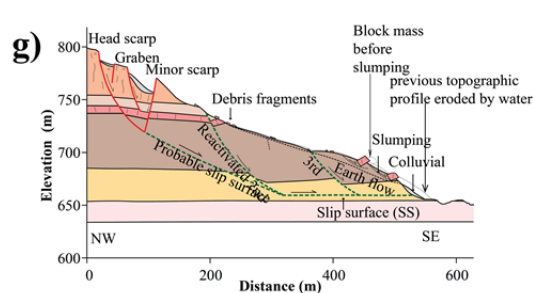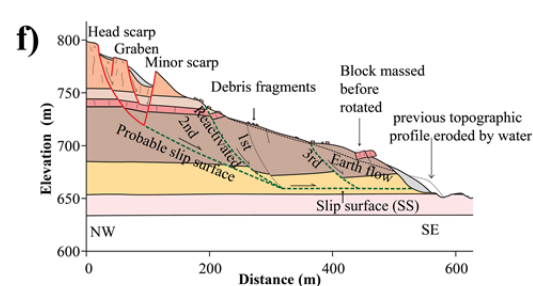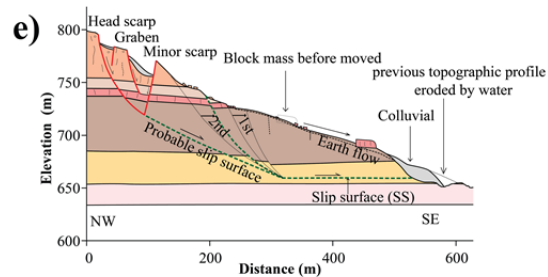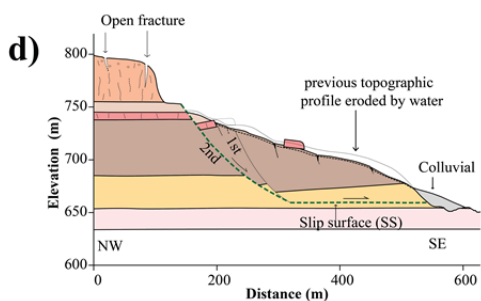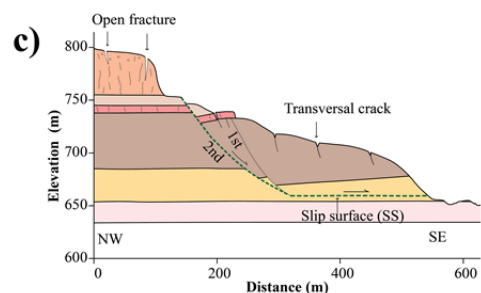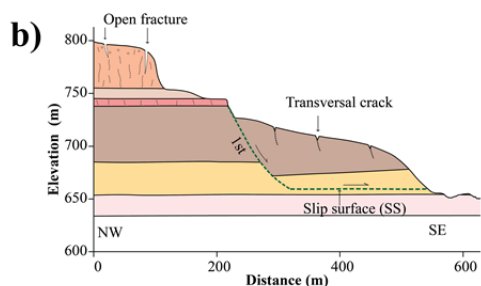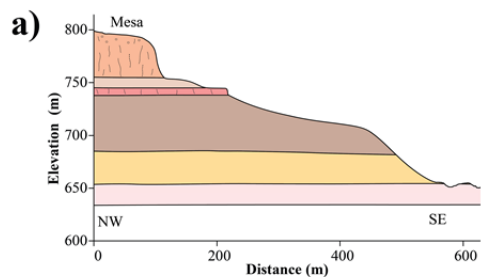
Explanation :

Colluvial deposits

Active Channel Deposits

Fluvial Terraces Deposits

Series of upper light gray and red brown basalt

Upper conglomeratic sandstone

Middle red brown basalt

Lower conglomeratic sandstone

Lower light gray greenish basalt

Clayey sandstone

Pumiceous sandstone

Fault

Slump, suspected

Slip surface, suspected

Figure 35. Diagram showing the simple model of the slope failure of the Black Canyon City landslide. (a) Initial topography, prior to landsliding. (b) The removal of material at the base by the bounding channels triggers the first slide along the curve-planar slip surface at the base. (c) The slip surface propagates backward causing translational and rotational movement along the main lobe and toe. (d) Block mass of the middle basalt unit in the main lobe is then transported downslope through hillslope processes. (e) The joints within the basalts grow into open fractures and propagate to the subsurface provide a pathway for water to infiltrate the subsurface causing small translational slides along the head and main lobe through planar surface and the merge into the planar surface at the base of the slide. (f) The slide moves the body southward by translation (with slight rotation). (g) Slumping moves another block mass of basalt and causing it to tilt to the north due to the slope instability at the toe. (h) Present configuration.

Future Movement and Hazard Assessment

The BCC landslide is located about ~ 650 m east of Interstate highway 17. Some structures are situated along two rivers that flow from north to south passing through the landslides region and flowing into Agua Fria River. The settlement is located ~750 m south of the landslide. The highway will not be interfered by the slide movement because the landslide movement is relatively parallel and away from the highway (to the south), but the settlement along the stream and the Agua Fria River may be in danger if the landslide moved significantly in the future.

The over steepened topographic slope at the toe indicates that the slide is in steady state condition, where the steepening of the slope is dominated by erosion process rather than slide acceleration. Our calculation of the landslide velocity indicates a velocity of 0.013-0.049 m/yr which according to landslide velocity classification of Cruden and Varnes (1996) is considered as inactive slide.

The morphology and geologic condition indicate that the landslide does not pose a hazard to the surrounding area of the Black Canyon City. Despite the steep south face of

the slide, the topographic slope tends to decrease over the time by the surface processes as shown by the presence of rills and gullies throughout the active lobe.

From the field observation, the streams surrounding the slide are not filled with standing water or for long period of time during storm, so it is hard for water to invade the clayey sandstone unit horizontally and reactivate the slip surface. However, extreme weather conditions may allow this to happen. The slide could collapse and feed debris flows which could flow to the settlement area. However, the volume of the material is relatively small to significantly affect the larger Black Canyon City area, except for several settlements near and along the stream below the toe of the slide.

CHAPTER 5

CONCLUSION

We have characterized the Black Canyon City landslide in Arizona using remote and field based mapping techniques aided by a high resolution DEM and orthophoto derived from Structure from Motion techniques. Our study indicates that the landslide motion is translational with slight rotational character. The slide has moved as a complex mass with at least two stages. The east-west trending head scarps indicate north-south extension as the slide mass moves south with some internal deformation. Shortening along the southern portion is indicated by topographic warping. The slip surface is estimated to be within the clayey sandstone units. The surface displacement velocity is considered as slow: ~10-60 mm/yr motion from 1998 to 2016. The surface displacement velocity from comparison of visual image from airphotos between a1930 and 1998 is ~0.1-3.6 m/yr. The slide motion is probably driven during wet periods when the mass is relatively heavier due to increased saturation and the basal slip surface weakened. The lack of topographic support due to landscape lowering along the bounding streams localizes the slide and enables its southward motion. The slide is stable and apparently does not pose significant hazard for the surrounding area given no extreme changes in the environmental condition.

Although the landslide is categorized as slow, monitoring the landslide is still necessary. We suggest to continue the monitoring effort and continue acquiring high resolution topographic dataset every five years or so to detect any surface displacement. We also suggest continuing surveying the stations using differential GPS that has good accuracy in the 3D perspective. Longer term rates of motion may be estimated with

additional field work and application of relevant geochronology for dating of deformed

surfaces or broken materials.

REFERENCES

Ayoub, F., Leprince, S., & Keene, L. (2009). User's Guide to COSI-CORR Co-registration of Optically Sensed Images and Correlation. *California Institute of Technology, Pasadena*.

Barbarella, M., Fazio, C., & Fiani, M. (2000). Evaluation of landslide volume using photogrammetric techniques. *Int Arch Photogramm Remote Sens*, *33*, 278-282.

Barlow, J., Martin, Y., & Franklin, S. E. (2003). Detecting translational landslide scars using segmentation of Landsat ETM+ and DEM data in the northern Cascade Mountains, British Columbia. Canadian journal of remote sensing, 29(4), 510-517.

Brardinoni, F., Slaymaker, O., & Hassan, M. A. (2003). Landslide inventory in a rugged forested watershed: a comparison between air-photo and field survey data. Geomorphology, 54(3), 179-196.

Highland, L., & Bobrowsky, P. T. (2008). The landslide handbook: a guide to understanding landslides (p. 129). Reston, VA, USA: US Geological Survey.

Brunsden, D., & Prior, D. B. (1984). Slope instability.

Cheok, G. S., Leigh, S., & Rukhin, A. (2002). Calibration experiments of a Laser Scanner. *NASA STI/Recon Technical Report N*, *2*, 88658.

Coney, P. J., & Reynolds, S. J. (1977). Cordilleran benioff zones. Nature, 270, 403-406.

Cruden, D. M., & Varnes, D. J. (1996). Landslides: investigation and mitigation. Chapter 3-Landslide types and processes. Transportation research board special report, (247).

Dikau, R. (1996). Landslide recognition: identification, movement, and clauses (No. 1). Wiley.

Doneus, M., Verhoeven, G., Fera, M., Briese, C., Kucera, M., & Neubauer, W. (2011). From deposit to point cloud‐a study of low-cost computer vision approaches for the straightforward documentation of archaeological excavations. Geoinformatics FCE CTU, 6, 81-88.

Verhoeven, G., Doneus, M., Briese, C., & Vermeulen, F. (2012). Mapping by matching: a computer vision-based approach to fast and accurate georeferencing of archaeological aerial photographs. Journal of Archaeological Science, 39(7), 2060-2070.

EPOCH (European community programme). (1993). Temporal occurrence and forecasting of landslide in the European community, (Ed.J-C.Flageollet). 3 volumes, Contract No. 90 0025

Ferguson, C.A., Haddad, D.E., Johnson, B.J., Guynn, J.H., Spencer, J.E., & David. L. Eddy, D.L. (2008). Geologic Map of the east half of the Black Canyon City 7 ½′ Quadrangle and the west half of the Squaw Creek Mesa 7 ½′ Quadrangle, Maricopa and Yavapai Counties, Arizona. *Arizona Geological Survey Digital Geologic Map DGM-64*

Fernandes, N. F., Coelho Netto, A. L., & Lacerda, W. A. (1994). Subsurface hydrology of layered colluvium mantles in unchannelled valleys—south-Eastern Brazil. *Earth Surface Processes and Landforms*, *19*(7), 609-626.

Haefeli, R. (1948). The stability of slopes acted upon by parallel seepage. In International Conference on Soil Mechanics and Foundation Engineering (pp. 57-62).

Glenn, N. F., Streutker, D. R., Chadwick, D. J., Thackray, G. D., & Dorsch, S. J. (2006). Analysis of LiDAR-derived topographic information for characterizing and differentiating landslide morphology and activity. *Geomorphology*, *73*(1), 131-148.

Guzzetti, F., Cardinali, M., & Reichenbach, P. (1996). The influence of structural setting and lithology on landslide type and pattern. *Environmental & Engineering Geoscience*, *2*(4), 531-555.

Highland, L., & Bobrowsky, P. T. (2008). The landslide handbook: a guide to understanding landslides (p. 129). Reston, VA, USA: US Geological Survey.

Hugenholtz, C. H., Moorman, B. J., Riddell, K., & Whitehead, K. (2012). Small unmanned aircraft systems for remote sensing and earth science research. *Eos, Transactions American Geophysical Union*, *93*(25), 236-236.

Johnson, K., Nissen, E., Saripalli, S., Arrowsmith, J. R., McGarey, P., Scharer, K., ... & Blisniuk, K. (2014). Rapid mapping of ultrafine fault zone topography with structure from motion. *Geosphere*, *10*(5), 969-986.

Leighty, R. S. (1997). Neogene tectonism and magmatism across the Basin and Range-Colorado Plateau boundary, central Arizona.

Leighty, R. S. (2007). Geologic map of the Black Canyon City and Squaw Creek Mesa area, central Arizona. Arizona Geological Survey.

Leprince, S., Barbot, S., Ayoub, F., & Avouac, J. P. (2007). Automatic and precise orthorectification, coregistration, and subpixel correlation of satellite images, application to ground deformation measurements. *Geoscience and Remote Sensing, IEEE Transactions on*, *45*(6), 1529-1558.

Lichti, D. D., Gordon, S. J., & Tipdecho, T. (2005). Error models and propagation in directly georeferenced terrestrial laser scanner networks. *Journal of surveying engineering*, *131*(4), 135-142.

Lucieer, A., de Jong, S., & Turner, D. (2013). Mapping landslide displacements using Structure from Motion (SfM) and image correlation of multi-temporal UAV photography. *Progress in Physical Geography*, 0309133313515293.

McKean, J., & Roering, J. (2004). Objective landslide detection and surface morphology mapping using high-resolution airborne laser altimetry.*Geomorphology*, *57*(3), 331-351.

Montgomery, D. R., & Buffington, J. M. (1997). Channel-reach morphology in mountain drainage basins. *Geological Society of America Bulletin*, *109*(5), 596-611.

Montgomery, D. R., Dietrich, W. E., Torres, R., Anderson, S. P., Heffner, J. T., & Loague, K. (1997). Hydrologic response of a steep, unchanneled valley to natural and applied rainfall. *Water Resources Research*, *33*(1), 91-109.

Nealey, L. D., & Sheridan, M. F. (1989). Post-Laramide volcanic rocks of Arizona and northern Sonora, Mexico, and their inclusions. Geologic Evolution of Arizona. Arizona Geological Society Digest. Arizona Geological Society, Tucson, 609-647.

Niethammer, U., James, M. R., Rothmund, S., Travelletti, J., & Joswig, M. (2012). UAV-based remote sensing of the Super-Sauze landslide: Evaluation and results. *Engineering Geology*, *128*, 2-11.

Pollard, D. D., and Fletcher, R. C., 2005, Fundamentals of Structural Geology, Cambridge University Press, 500 p

Prokešová, R., Kardoš, M., & Medveďová, A. (2010). Landslide dynamics from high-resolution aerial photographs: a case study from the Western Carpathians, Slovakia. Geomorphology, 115(1), 90-101.

Razak, K. A., Straatsma, M. W., Van Westen, C. J., Malet, J. P., & De Jong, S. M. (2011). Airborne laser scanning of forested landslides characterization: terrain model quality and visualization. *Geomorphology*, *126*(1), 186-200.

Rib, H. T., & Liang, T. (1978). Recognition and identification. Transportation Research Board Special Report, (176).

Rott, H. (2009). Advances in interferometric synthetic aperture radar (InSAR) in earth system science. Progress in Physical Geography.

Savigear, R. A. G. (1965). A TECHNIQUE OF MORPHOLOGICAL MAPPING 1. Annals of the Association of American Geographers, 55(3), 514-538.

Shafiqullah, M., Damon, P. E., Lynch, D. J., Reynolds, S. J., Rehrig, W. A., & Raymond, R. H. (1980). K-Ar geochronology and geologic history of southwestern Arizona and adjacent areas. Studies in western Arizona: Arizona Geological Society Digest, 12, 201-260.

Sidle, R. C. (1984). Shallow groundwater fluctuations in unstable hillslopes of coastal Alaska. *Zeitschrift fur Gletscherkunde und Glazialgeologie*, *20*.

Skempton, A. W., & Hutchinson, J. (1969). Stability of natural slopes and embankment foundations. In Soil Mech & Fdn Eng Conf Proc/Mexico/.

Spencer, J. E., & Reynolds, S. J. (1989). Middle Tertiary tectonics of Arizona and adjacent areas. Geologic evolution of Arizona: Arizona Geological Society Digest, 17, 539-574.

Tsuboyama, Y., Sidle, R. C., Noguchi, S., Mukarami, S., & Shimizu, T. (2000). A zero-order basin-its contribution to catchment hydrology and internal hydrological processes . *Hydrological Processes*, *14*, 387-401.

Turner, D., Lucieer, A., & de Jong, S. M. (2015). Time series analysis of landslide dynamics using an unmanned aerial vehicle (UAV). Remote Sensing, 7(2), 1736-1757.

Van Den Eeckhaut, M., Poesen, J., Verstraeten, G., Vanacker, V., Moeyersons, J., Nyssen, J., & Van Beek, L. P. H. (2005). The effectiveness of hillshade maps and expert knowledge in mapping old deep-seated landslides. Geomorphology, 67(3), 351-363.

Van Den Eeckhaut, M., Poesen, J., Govers, G., Verstraeten, G., & Demoulin, A. (2007). Characteristics of the size distribution of recent and historical landslides in a populated hilly region. Earth and Planetary Science Letters, 256(3), 588-603.

Van Westen, C. J., & Getahun, F. L. (2003). Analyzing the evolution of the Tessina landslide using aerial photographs and digital elevation models. Geomorphology, 54(1), 77-89.

Varnes, D. J. (1978). Slope movement types and processes. Transportation Research Board Special Report, (176).

Ventura, G., Vilardo, G., Terranova, C., & Sessa, E. B. (2011). Tracking and evolution of complex active landslides by multi-temporal airborne LiDAR data: the Montaguto landslide (Southern Italy). *Remote Sensing of Environment*,*115*(12), 3237-3248.

Verhoeven, G. (2011). Taking computer vision aloft‑archaeological three‑dimensional reconstructions from aerial photographs with photoscan. Archaeological Prospection, 18(1), 67-73.

APPENDIX A

ADDITIONAL ANALYSIS

1. Histogram analysis

I analyzed fracture orientation of the Black Canyon City landslide measured using aerial photos and in the field. I use Stereonet8 (http://www.geo.cornell.edu/geology/faculty/RWA/programs/stereonethtml) to plot and analyze the trends of the fractures. The plot show that the fractures are mainly in N-S orientation. The N-S trending fractures are mainly located within the main lobe while the E-W are along the head and the SE lobe.
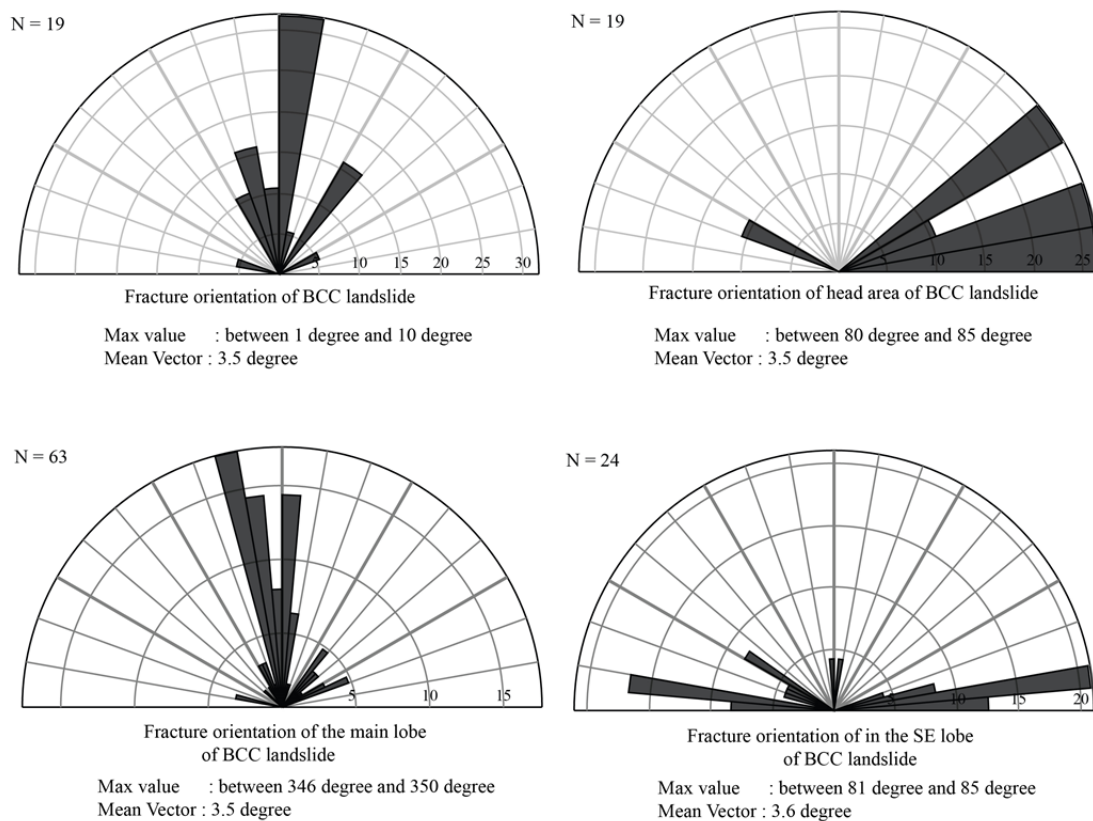

Figure 36. The rose diagram of the trend of fractures measured in the BCC landslide, the upper left is all the trends, upper right is fracture at the head area, the lower left on the main lobe, lower right on the SE lobe.

2. Surface rupture calculation

To estimate the amount of displacement of the opening fractures, I measured the component of the displacement: the fracture-normal, fracture-parallel in the horizontal plane, and the vertical. The measured parameters and the estimation of the magnitude of displacement are shown in table 11.

Table 11. Measurement of the displacement parameters and calculation of the amount of displacement of opening fractures in the BCC landslide

FID	Shape	X-Coordinate	Y-Coordinate	Z-Elev	station	horizontal	parallel	vertical	Net Slip	Trend line	Strike Orientation (N...E)	Ψ (psi)	Trend (Ο)	Trend (Ο)	r-direction	Dip Slip	Pitch (Ω)(strike slip/net slip)	Apparent rake (β)	angle ECA (plunge)
1	point	395521.108	3772881.448	701.593994	103	22	45	53	72.9	50.1	15	64	79	79	E-S	69.5	72.4	17.6	46.6
2	point	395521.513	3772880.408	701.593994	103a	1.5	6.5	0.8	6.7	6.7	70	77	147	147	S-W	6.5	77.1	12.9	6.8
3	point	395521.508	3772881.947	701.593994	103b	1.5	5.5	1	5.8	5.7	125	75	200	200	S-W	5.6	75.0	15.0	9.9
4	point	395517.931	3772902.776	702.526733	104	2.5	20	2.4	20.3	20.2	356	83	439	79	E-S	20.1	82.9	7.1	6.8
5	point	395512.018	3772910.383	708.862976	105	1.5	5	8	9.6	5.2	329	73	402	42	E-S	9.4	81.0	9.0	56.9
6	point	395517.18	3772909.993	709.650391	106	11	15.5	3.8	19.4	19.0	332	55	387	27	E-S	16.0	55.4	34.6	11.3
7	point	395521.291	3772914.605	709.650391	107	7.5	6.5	2.5	10.2	9.9	335	41	376	16	E-S	7.0	42.9	47.1	14.1
8	point	395506.428	3772930.518	712.346436	108	8	32	30	44.6	33.0	342	76	418	58	E-S	43.9	79.7	10.3	42.3
9	point	395507.375	3772966.00	723.794739	79	1.5	19	0.8	19.1	19.1	345	85	430	70	E-S	19.0	85.5	4.5	2.4
10	point	395488.249	3772938.593	717.009277	111	2	7	0.9	7.3	7.3	348	74	422	62	S-W	7.1	74.2	15.8	7.0
11	point	395483.48	3772957.832	721.456055	78a	1.4	6.5	0.8	6.7	6.6	352	78	430	70	S-W	6.5	77.9	12.1	6.9
12	point	395484.28	3772957.832	721.456055	78b	2	9.5	16.5	19.1	9.7	345	78	423	63	S-W	19.0	84.0	6.0	59.5
13	point	395484.9	3772957.832	721.456055	78c	1.4	11	1	11.1	11.1	335	83	418	58	S-W	11.0	82.8	7.2	5.2
14	point	395485.69	3772957.832	721.456055	78d	2.5	19	3.5	19.5	19.2	355	83	438	78	S-W	19.3	82.6	7.4	10.4
15	point	395486.48	3772957.832	721.456055	78e	1.5	6	1	6.3	6.2	350	76	426	66	S-W	6.1	76.2	13.8	9.1
16	point	395487.597	3772957.832	721.456055	78f	1	9.5	1	8.5	8.4	348	83	431	71	S-W	9.6	83.2	6.8	6.8
17	point	395475.369	3772966.905	726.418579	113	4	21	3.5	21.7	21.4	25	79	104	104	E-S	21.3	79.4	10.6	9.3
18	point	395458.418	3772985.946	729.824524	115	3.5	13.5	1.5	14.0	13.9	355	75	430	70	S-W	13.6	75.6	14.4	6.1
19	point	395454.608	3772975.12	725.456238	76a	3	9	2.5	9.8	9.5	350	72	422	62	S-W	9.3	72.2	17.8	14.8
20	point	395456.625	3772975.12	725.456238	76b	5.5	18	8	20.5	18.8	352	73	425	65	S-W	19.7	74.4	15.6	23.0
21	point	395423.106	3772988.223	735.708984	116	5.5	9	50	51.1	10.5	6	59	65	65	S-W	50.8	83.8	6.2	78.1
22	point	395449.503	3772989.04	736.480164	117	3	8	2.2	8.8	8.5	12	69	81	81	S-W	8.3	70.1	19.9	14.4
23	point	395429.068	3772968.417	734.514648	118a	3	8.5	0.5	9.0	9.0	4	71	75	75	S-W	8.5	70.6	19.4	3.2
24	point	395428.158	3772968.617	734.514648	118b	1.5	16	8	18.0	16.1	6	85	91	91	S-W	17.9	85.2	4.8	26.5
25	point	395427.248	3772968.737	734.514648	118c	2	8.5	0.5	8.7	8.7	5	77	82	82	S-W	8.5	76.8	13.2	3.3
26	point	395432.633	3772965.383	733.99408	119	3.5	9.5	0.5	10.1	10.1	10	70	80	80	S-W	9.5	69.8	20.2	2.8
27	point	395430.283	3772953.21	734.311157	120	4	12	1	12.7	12.6	8	72	80	80	S-W	12.0	71.6	18.4	4.5
28	point	395410.564	3773005.441	739.199402	121a	1.5	30	0.7	30.0	30.0	342	87	429	69	E-S	30.0	87.1	2.9	1.3
29	point	395412.632	3773007.441	739.199402	121b	1	7.5	0.6	7.6	7.6	340	82	422	62	E-S	7.5	82.4	7.6	4.5
30	point	395391.937	3773039.695	749.208557	122	3	10	6	12.0	10.4	5	73	78	78	E-S	11.7	75.6	14.4	29.9
31	point	395430.033	3773105.369	760.38031	BCBR6	1.5	6	1	6.3	6.2	5	76	81	81	E-S	6.1	76.1	13.9	9.2
32	point	395455.088	3773076.701	753.520813	123	0.5	4.5	0.8	4.6	4.5	125	84	209	209	E-S	4.6	83.8	6.2	10.0
33	point	395539.742	3772955.989	708.836548	BCCCRCK2	0.5	3.5	0.5	3.6	3.5	275	82	357	357	S	3.5	82.0	8.0	8.0
34	point	395549.009	3772943.022	702.524048	BCCCRCK1	1	6	5.5	8.2	6.1	356	81	437	77	S-W	8.1	83.0	7.0	42.1
35	point	395561.223	3772904.514	724.751282	127	10	10	2	14.3	14.1	355	45	400	40	S-W	10.2	45.6	44.4	8.0
36	point	395479.879	3772941.015	717.704163	112	2.5	20	1.5	20.2	20.2	355	83	438	78	S-W	20.1	82.9	7.1	4.3
37	point	395510.647	3772953.206	703.623291	109A	5	14	6.5	16.2	14.9	105	70	175	175	S-W	15.4	72.1	17.9	23.6
38	point	395467.689	3772981.629	714.514893	128	6.5	15.5	11.5	20.4	16.8	35	67	102	102	S-W	19.3	71.4	18.6	34.4
39	point	395428.957	3772983.39	719.041199	129	4	11.5	5	13.2	12.2	25	71	96	96	S-W	12.5	72.3	17.7	22.3
40	point	395413.064	3772956.284	716.422668	130	6.5	43	15	46.0	43.5	8	81	89	89	S-W	46.1	81.9	8.1	19.0
41	point	395408.822	3772956.553	717.067383	131	6	17	66	68.4	18.0	8	71	79	79	E-S	68.2	85.0	5.0	74.7
42	point	395409.739	3772980.941	722.415466	BCCB1	19	56	94	111.1	59.1	11	71	82	82	E-S	109.4	80.1	9.9	57.8
43	point	395410.431	3773143.182	757.198914	135	5.5	8	35.5	36.8	9.7	282	55	337	337	N-W	36.4	81.4	8.6	74.7
44	point	395426.786	3773161.965	766.521057	136	1.5	21	0.6	21.1	21.1	35	86	121	121	N-W	21.0	85.9	4.1	1.6
45	point	395378.068	3773161.729	760.277222	138	0	18	14	22.8	18.0	260	90	350	350	N-W	22.8	90.0	0.0	37.9
46	point	395783.478	3773078.499	691.117188	80	5.5	16.5	20	26.5	17.4	118	72	190	190	S-W	25.9	78.0	12.0	49.0
47	point	395785.685	3773077.809	689.576721	81	4.5	19	5	20.2	19.5	120	77	197	197	S-W	19.6	77.1	12.9	14.4
48	point	395808.953	3773137.772	711.196167	82	2.5	18.5	1.5	18.7	18.7	120	82	202	202	S-W	18.6	82.3	7.7	4.6
49	point	395800.532	3773135.536	712.200256	83	10.5	23.5	5.5	26.3	25.7	118	66	184	184	S-W	24.1	66.5	23.5	12.1
50	point	395794.307	3773131.612	713.633484	84	0	37	0	37.0	37.0	120	90	210	210	S-W	37.0	90.0	0.0	0.0
51	point	395784.48	3773135.713	716.541565	85	13.5	56	3.5	57.7	57.6	240	76	316	316	E-N	56.1	76.5	13.5	3.5
52	point	395782.395	3773139.063	718.348938	86	6	21.5	3.5	22.6	22.3	245	74	319	319	E-N	21.8	74.6	15.4	8.9
53	point	395744.251	3773143.921	724.074829	87	0	57	0	57.0	57.0	116	90	206	206	S-W	57.0	90.0	0.0	0.0
55	point	395727.166	3773243.48	723.596714	95	10	102	0	102.8	102.8	170	79	249	249	S-W	102.0	79.4	10.6	0.0

3.   InSAR displacement analysis

An unpublished data of InSAR analysis over Black Canyon City landslide during
2011 – 2013 is available to support this study. The analysis was performed by Jeffrey
Moore of University of Utah
(*https://twitter.com/UtahGeohaz/status/705108780040613888/photo/1?cn=cmVwbHk%3*
D&refsrc=email). He suggest that this site is not active during period time (2012-2013)
as indicated by the uniform of green color occurred over the BCC landslide area
(representing the absent of displacement) in Figure 37.
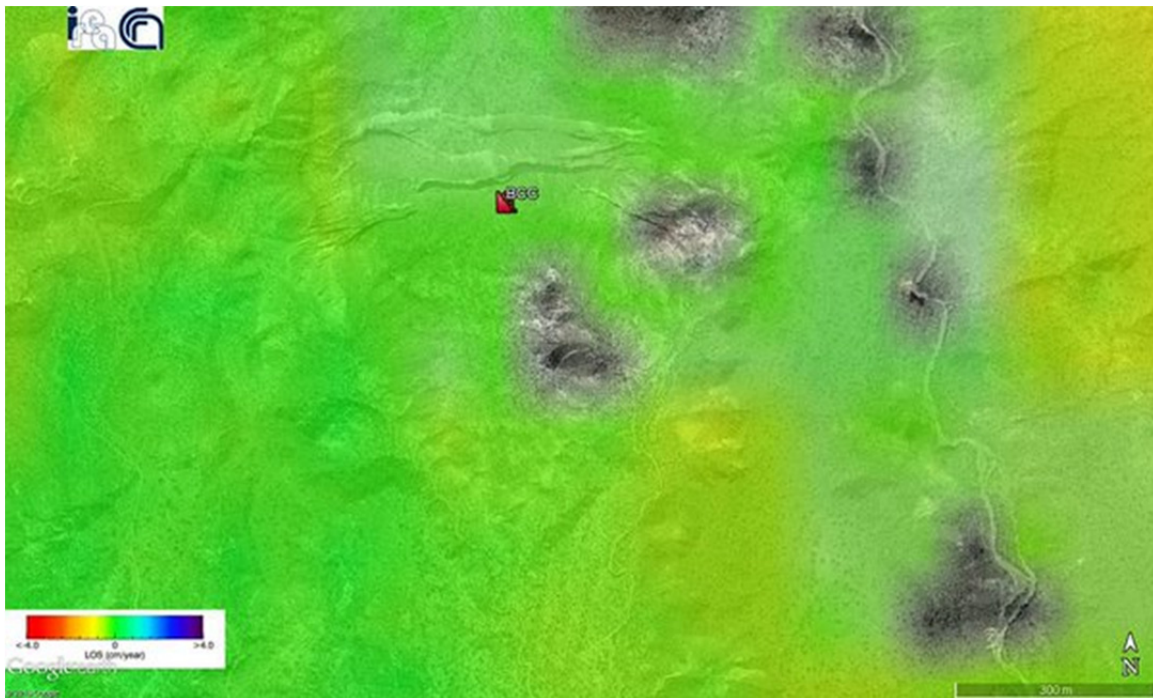
Figure 37. InSAR displacement analyis of the Black Canyon City landslide, green color
represent zero displacement.

4.   Georeferencing Method

To quantify the surface displacement from 1930 to 1998, I qualitatively compared the1930 and 1998 aerial photos in ArcGIS. I delineate the features identifiable on both images, which include: scarp, toe, and lithology boundary. The aerial photos were georeferenced in ArcGIS prior to the interpretation. I georeferenced the 1998 photo using our orthophoto generated by the SfM processing (see Figure 38) while the 1930 is georeferenced to the 1998 aerial photograph. We georeferenced the 1930 photo to the 1998 photo because their resolutions are similar and thus features are easily correlated. I used 4 prominent morphological features (sharp bend of the channel, hillslope top and lithologic boundaries) as piercing points (Figure 38 and 39). The piercing points were chosen from area outside of the landslide as they are considered stable. I use the 1st order polynomial (affine) as the georeferencing transformation to meet the accuracy of our data. The total RMSE is ~ 6.7 for the 1998 and orthophoto and ~ 15.7 for the 1998 and 1930 of airphoto (see Figure 38 and 39 for details).
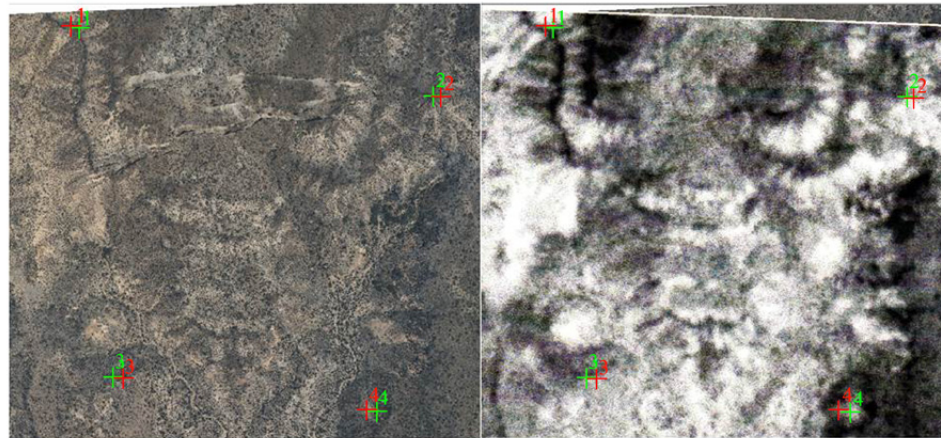
Figure 38. georeferenced points between 1998 airphoto and our orthophoto, where the orthophotos is considered as reference imagery

Figure 39. georeferenced points between 1930 and 1998 airphotos, where the 1998 airphotos is considered as reference imagery

APPENDIX B

BENCHMARK INFORMATION

1. **Benchmark photos and newly acquired coordinate measured using dGPS instrument**

I inspect the condition and measured the locations of all the benchmarks. The majorities of the benchmarks is still well-preserved and are in their original location, but few of them were appear to be moved from their original position (the instrument station and BM 28). One of the benchmark is missing its name tag. I present documentation from 1998 and 2016 to compare their condition and location.

Figure 40. Photo of BM 1 taken in 1998

Figure 41. Photo of BM 1 taken in 2016

No photo of BM2 taken in 1998

Figure 42. Photo of BM 2 taken in 2016

Figure 43. Photo of BM 5 taken in 1998

Figure 44. Photo of BM 5 taken in 2016

No photo of BM6? taken in 1998

Figure 45. Photo of BM 6? Taken in 2016, not sure this is the real benchmark name

Figure 46. Photo of BM 8 taken in 1998

Figure 47. Photo of BM 8 taken in 2016

No photo of BM 25 taken in 1998

Figure 48. Photo of BM 25 taken in 2016

No photo of BM 27 taken in 1998

Figure 49. Photo of BM 27 taken in 2016

Figure 50. Photo of BM 28 taken in 1998

Figure 51. Photo of BM 28 taken in 2016

Figure 52. Photo of BM 10 taken in 1998

Figure 53. Photo of BM 10 taken in 2016

Figure 54. Photo of BM 19 taken in 1998

Figure 55. Photo of BM 19 taken in 2016

No photo of BM 11 taken in 1998

Figure 56. Photo of BM 11?, there is no initial name of the benchmark, taken in 2016

Figure 57. Photo of BM 18 taken in 1998

Figure 58. Photo of BM 18 taken in 2016

No photo of BM 17? taken in 1998

Figure 59. Photo of BM 17?. there is no indication of benchmark name, taken in 2016

No photo of instrument station taken in 1998

Figure 60. Photo of Instrument station, where the benchmark has been relocated from the original places

Table 12. New coordinate of benchmark station generated from dGPS measurement, Zone 12, WGS 1984

No	Benchmark	Latitude			Longitude			East	North	Elevation
		degrees	minutes	seconds	degrees	minutes	seconds			
1	BM1	34	5	21.76903	112	7	55.8066	395553.9278	3772645.751	620.489
2	BM2	34	5	23.73628	112	7	57.12059	395521.2715	3772704.669	620.488
3	BM5	34	5	25.13196	112	7	56.75684	395529.4978	3772747.608	628.488
4	BM5?	34	5	25.52687	112	7	56.46228	395537.2927	3772759.942	630.181
5	BM8	34	5	26.12588	112	7	57.29928	395517.0157	3772778.577	640.953
6	BM25	34	5	27.17488	112	7	59.72466	395455.8569	3772813.19	648.309
7	BM27	34	5	31.7863	112	8	1.64271	395408.7177	3772955.445	671.925
8	BM8	34	5	32.26546	112	7	59.52104	395462.7654	3772970.261	674.034
9	BM10	34	5	32.14563	112	7	57.90131	395503.6576	3772963.597	674.103
10	BM19	34	5	32.01481	112	7	56.55089	395536.9271	3772960.123	673.38
11	BMA0	34	5	37.20491	112	7	50.70488	395689.9053	3773118.682	699.544
12	BM18	34	5	42.63225	112	7	56.9672	395532.8886	3773286.773	756.957
13	BM28	34	5	32.26588	112	7	59.52103	395462.7654	3772970.261	674.038
14	BM14	34	5	25.13104	112	7	56.75756	395529.4991	3772747.719	628.491
15	BM17	34	5	32.10083	112	7	49.65826	395713.8136	3772961.27	632.249
16	intrument station	34	5	19.80114	112	7	46.82061	395783.8907	3772581.546	647.218
17	Station dgps	34	5	22.29322	112	7	49.12661	395725.7899	3772659.265	633.324